university of groningen

faculty of science
and engineering

MASTER'S THESIS

Interactions of heavy, low-energy ions with a Ru surface

Author:
Zafer Nur
s5306418

Examiners:
Prof. dr. ir. R. Hoekstra
Dr. A. Grubisic-Cabo
Ir. L. Assink

March 26, 2024

Submitted to fulfill the requirements for
the degree of
Master of Science
in
Applied Physics

Abstract

The interactions between Xe ions in the keV-energy regime and a Ru surface have been studied. The light sources of the modern EUV lithography machines create Sn-ion debris, which may collide with EUV optics and damage them. Previous attempts to understand the interaction between a Sn ion beam and transition metal surfaces such as Mo and Ru, using the Binary Collision Approximation (BCA) have ended up with a discrepancy: the absence of a single collision peak in the scattering energy spectrum. The aim of this thesis is to test to what extent the BCA works for explaining ion surface interactions by using Xe, another element heavier than Ru, as a projectile, and to see whether this discrepancy is specific to Sn or if it is about being heavier than the target atoms. The experiments are conducted by hitting a surface with an ion beam obtained from an ECR ion source at the Zernike Low-Energy Ion Facility (ZERNIKELEIF) at the University of Groningen. As a result of the experiments, it has been observed that the intensities of all peaks decrease as the initial energy of the beams increases. The recoil peaks are dominant in the spectra for all beams with different energies. Another series of experiments has been performed with the same initial energy, but different initial charge states, and it shows that the initial charge state does not have a significant effect on the shape and overall counts of the resulting spectra. In conclusion, between the predictions of BCA and the experimental results, a fairly good match is found. However, the projectiles being heavier than the target atoms causes the recoil peak to be so intense that the SC peak appears to be hidden underneath the recoil peak.

Contents

1 Introduction

The technological driving force of modern life is based on electronic devices. The demand for more advanced electronics requires the ability to contain more transistors in smaller integrated circuits (ICs) (see figure 1.1 for a generic IC). Efforts to make more powerful microchips have enabled new techniques, while presenting the semiconductor industry with new difficulties. Although extreme ultraviolet (EUV) lithography, the new frontier for making smaller ICs, offers extraordinary solutions for more powerful chips, it poses new challenges. The EUV light that is needed for these machines is generated from laser-produced plasma of Sn, but the generation of EUV light creates debris that may hit and damage plasma-facing material and equipment. The debris contains Sn ions, atoms, and Sn particles several micrometers in diameter with energies up to several keV [1, 2]. To protect the lifetime of the plasma-facing equipment, a profound understanding of interactions between the surfaces and Sn debris is important.

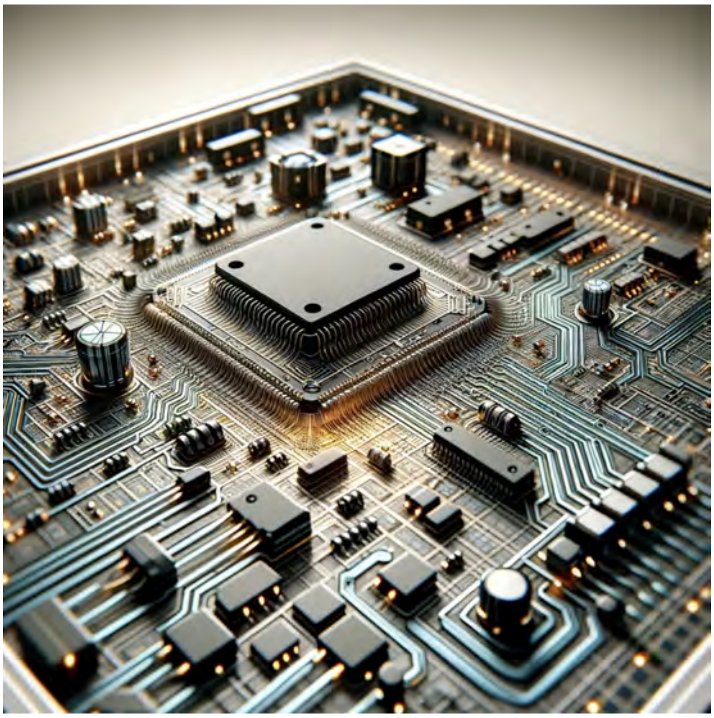

Figure 1.1: An integrated circuit illustration.

The Binary Collision Approximation (BCA) theory foresees a single collision (SC) peak in the energy distribution of Sn ions scattered on a Ru target. However, the previous experimental studies [1, 3] could not demonstrate the SC peak in their results. In these works, they also ran simulations using the Stopping and Range of Ions in Matter (SRIM) software. The experimental results and simulations were in agreement, except for the SC peak. Rai et al. have investigated Kr^+ as a projectile on a Cu target, as it has the same mass ratio as in the Sn-Ru experiments, to show if a different projectile and target combination might explain the apparent absence of the peak [4]. They demonstrated SC peaks only for small scattering angles with low intensities, unlike SRIM simulations, which yield SC peaks for all possible angles. Assink et al. have performed experiments with Ar, Kr, and Xe as projectiles on a Ru target with different initial energies and charge states [5]. They have shown that the SC peak becomes visible for a lighter projectile.

Based on these recent findings, further investigation should focus on the effects of initial energies and charge states. In this study, backscattering experiments are performed with Xe beams with different charge states that have energies ranging from 5 to 60 keV. The experiments are performed at the Zernike Low-Energy Ion Facility (ZERNIKELEIF) at the University of Groningen. Ion beams are created from plasmas in a supernanogan-type Electron Cyclotron Resonance Ion Source (ECRIS). The collisions between the ion beams and a target surface take place in a UHV chamber called SirPhi (Surface Physics setup). The setup has two different detector systems to collect data from collision experiments: an electrostatic analyzer (ESA) in the collision chamber and three time-of-flight (ToF) tubes mounted at different angles. Furthermore, the SRIM software package was used to simulate one of the experiments with the same beam energy and collision geometry. The aim of this research is to understand why there is a discrepancy between the experiments and BCA prediction when the projectile is heavier than the target atom. Furthermore, comparing the energy distributions of reflected and recoiled particles with different energies and charge states can provide not only a more in-depth understanding of ion surface interactions but also benchmark possibilities for the SRIM-like simulation packages.

This thesis consists of five chapters. Chapter 2 comprises the theoretical foundation. In this chapter, the BCA and scattering cross-section will be discussed. The experimental setup and simulation software package, SRIM, will be explained in Chapter 3. ZERNIKELEIF, ECRIS, the beamline and their components, the structure of the SirPhi, and the detectors, ESA and ToF tubes, used for data collection throughout the experiments will be the subsections of Chapter 3. The results and discussion will take place in Chapter 4, in which we will focus on the influence of the initial energy and initial charge state and discuss ToF results as well. To conclude, in Chapter 4, a comparison between the experiments and the simulation is given.

2 Theory

The interaction between an ion beam and a surface bombarded by it represents a many-body problem. Since a many-body problem is quite complex to solve and analyze, they must be simplified to a two-body problem. This means that ion-surface interactions can be treated by isolating each collision in a pairwise manner. The assumption that the interaction between the two atoms is properly described by a simple elastic collision of two isolated particles rests on two conditions [6]:

1. The projectile energy E_0 must be much larger than the binding energy of the atoms in the target. Chemical bonds are of the order of 10 eV, so that E_0 should be very much larger than that.
2. Nuclear reactions and resonances must be absent.

In the energy regime of tens of keV, these two conditions are well satisfied. Therefore, the scattering of particles from a surface can be described by using so-called Binary Collision Approximation (BCA).

2.1 Binary Collision Approximation

The BCA allows us to treat the ion-surface interaction as if it were a collision between two solid balls. Figure 2.1a shows the geometry of the BCA. Once a projectile collides with a target atom at rest, its trajectory deviates from the initial direction with a scattering angle of θ. During the collision event, a part of the projectile's kinetic energy is transferred to the target atom. Inelastic collisions and their results are not subject to this study and, thereby, this discussion. Since the collision is assumed to be elastic, the kinematics of the collision event can be analyzed using the conservation laws of energy and momentum:

$$\frac{1}{2}m_p v_0^2 = \frac{1}{2}m_p v_p^2 + \frac{1}{2}m_t v_t^2, \tag{2.1}$$

$$m_p v_0 = m_p v_p cos\theta + m_t v_t sin\phi, \tag{2.2}$$

$$0 = m_p v_p sin\theta + m_t v_t sin\phi. \tag{2.3}$$

The goal of the kinematic analysis is to obtain the ratios E_f/E_0 and E_{rec}/E_0, i.e., to determine the amount of energy retained by a projectile or transferred to a target atom. Rearranging equation 2.2 and using equation 2.3, v_p/v_0 is obtained and can be transformed to E_f/E_0:

$$\frac{E_{f\pm}}{E_0} = \left(\frac{\cos\theta \pm \sqrt{(m_t/m_p)^2 - \sin^2\theta}}{1 + m_t/m_p}\right)^2. \tag{2.4}$$

When $m_p < m_t$, the E_{f+}/E_0 is the only solution. Throughout this thesis, since $m_p > m_t$, the subscript ± indicates that there are two solutions for the final energy of the projectile, E_f, each corresponding to the positive or negative sign of the square root in the equation 2.4. Moreover, the equation 2.4 is symmetric in the scattering angle, θ. The part of the equation with square root can become negative when $m_p > m_t$, and puts a maximum limit on scattering angle:

$$\theta_{max} = \arcsin\left(\frac{m_t}{m_p}\right). \tag{2.5}$$

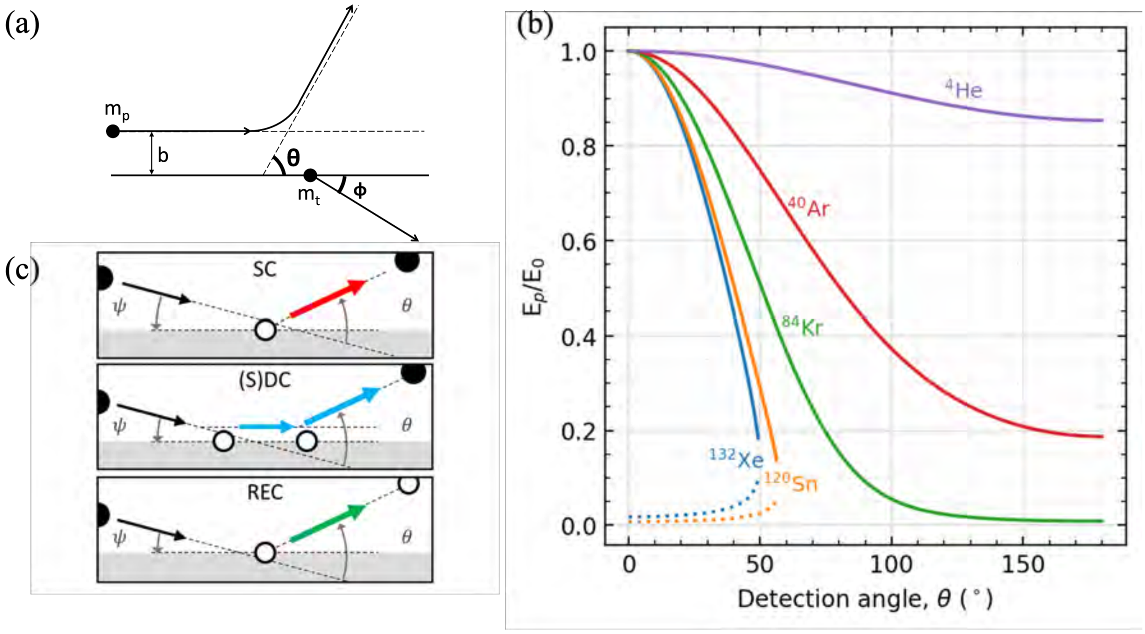

Figure 2.1: The geometry of a binary collision with b, the impact parameter, the scattering angle of θ and the recoil angle of ϕ **(a)**. Energy proportions of the reflected particles versus the scattering angles with different projectiles on ^{101}Ru target. For Xe and Sn, the solid lines are (+) solutions and the dashed lines are (-) solutions of equation 2.4 **(b)**. Different possibilities, single and double collision and recoil, on a target surface **(c)**.

When the target atom is lighter than the projectile, it can only transfer a certain fraction of its momentum to the extent that this mass ratio allows, and thus a maximum scattering angle emerges. Since the experiments in this study are performed with Xe ions and Ru target, and $m_{Xe} > m_{Ru}$, there is a maximum scattering angle θ_{max} of 49.9°.

By performing similar steps as in E_f/E_0, the proportion of E_{rec} to E_0 can be written as

$$\frac{E_{rec}}{E_0} = \frac{4m_t m_p}{(m_t + m_p)^2}\cos^2\phi. \tag{2.6}$$

Equation 2.6 has only one solution in the case of an elastic collision, unlike the equation 2.4, which has two solutions. Furthermore, the recoil angle, ϕ, can only take values between -90° and 90°; otherwise, the E_{rec}/E_0 ratio becomes negative. A target particle can thus only recoil into a half-sphere of solid angle with respect to the direction of the incoming projectile.

For different scattering angles after a collision event, figure 2.1b shows the amount of energy retained by the projectile. Projectiles that are lighter than the target atoms, ^{4}He, ^{40}Ar and ^{84}Kr, have a continuous curve for scattering angles from 0 to 180 degrees. On the other hand, the curves of projectiles that are heavier than the target atoms are cut off at the maximum scattering angle predicted by equation 2.5. Therefore, measurements at a detection angle larger than θ_{max} do not contain SC events, but only multiple collision and recoil events. The dotted parts of the curves of Xe and Sn correspond to the negative solutions of the equation 2.4.

In figure 2.1c, we present different ways in which a projectile can scatter from a target surface, or a target atom can be sputtered. In the first case, the projectile collides with a target atom at or near the surface, and does not encounter any other target atoms. Such a backscattering event is called a single collision. The energy of the projectile after a single collision will be the value predicted by equation

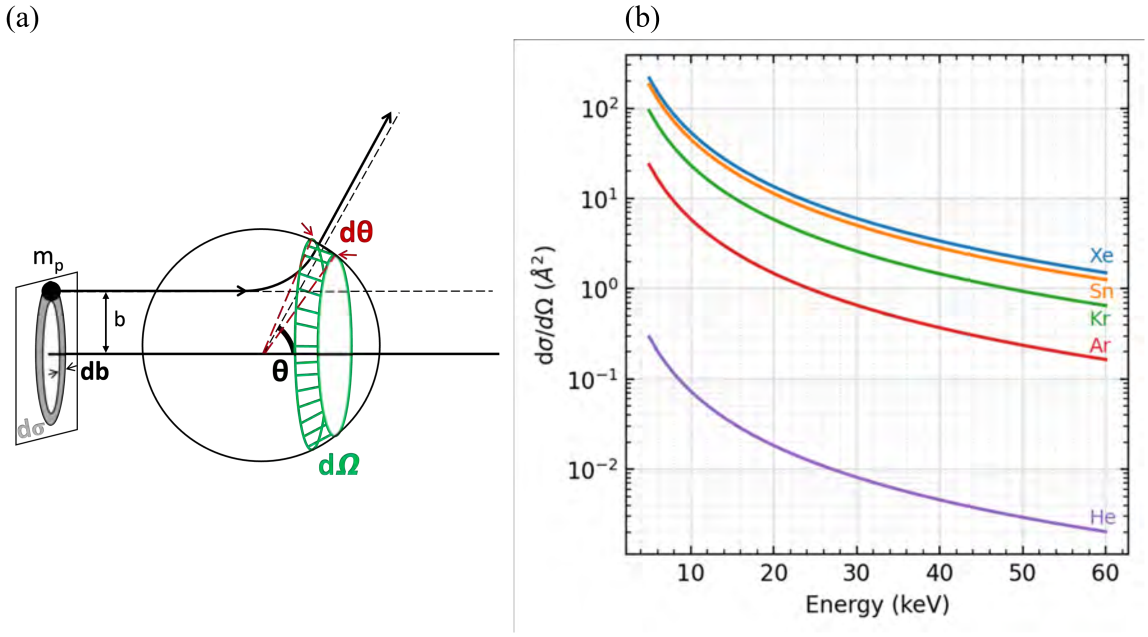

Figure 2.2: Schematic layout of a collision event, showing a portion of an incoming beam, db, and the solid angle, dΩ, at which the portion of the incoming beam is scattered **(a)**. Differential cross-section values for different projectiles versus energies ranging from 5 to 60 keV **(b)**.

2.4. In other cases, multiple collisions can take place. A double collision (DC) event can occur over two collisions, before leading to a certain overall scattering angle ($\theta_{det} \neq \theta$). A triple collision is also possible, causing scattering at a certain angle. For a measurement over a detection angle, θ_{det}, of 40°, double collision events can emerge with combinations of collisions, e.g., over 10° plus 30°, or 20° plus 20°. When a double collision event occurs over the same two scattering angles, this is called a symmetric double collision (SDC) event ($\theta_{det} = 2\theta$). The other special case of a multiple collision is called a quasi-single collision. The projectile can experience one collision over a large scattering angle, combined with multiple small scattering angle collisions. When the projectile has a quasi-single collision, it retains slightly more energy than a single collision event. The energy transferred by the projectile to a target atom (recoils) can overcome the lattice binding energy, and the target atom can leave the surface eventually. This is defined as primary recoil. These three possibilities can be seen in the energy distribution at different energies. It should be noted that the recoils are not plotted as their energy fraction is given as $(1 - E_f/E_0)$. For example, a Xe projectile experiencing an SC on a Ru target will retain 45% of its initial energy for a measurement at 40°. For an SDC, a reflected particle with two collisions over 20° will keep 72% of its initial energy. Multiple collision events are one of the reasons that widen the SC and (S)DC peaks with different combinations of angles and the number of pre-scattering collision events. Other reasons can be different isotopes of the target atoms and detector opening angle, which can lead to slightly different detection angles.

2.2 Differential Scattering Cross-section

The scattering angle is determined by the impact parameter, b [1]. There is an inverse relation between the impact parameter and the scattering angle; the larger the impact parameter, the smaller the scattering angle [7]. The probability that a reflected or recoiled particle is detected at an arbitrary scattering angle is given by the differential scattering cross-section. In figure 2.2a, the number of particles inside the annulus area, $d\sigma$ with the thickness db, ideally will scatter into the solid angle $d\Omega$. If a Coulomb field is taken as a scattering force field, the differential scattering cross-section in the laboratory system is given by Rutherford's formula [6, 8]:

$$\frac{d\sigma}{d\Omega} = \left(\frac{Z_p Z_t e^2}{2E}\right)^2 \frac{[\sqrt{1-(m_p/m_t)^2 \sin^2\theta} + \cos\theta]^2}{\sin^4\theta\sqrt{1-(m_p/m_t)^2\sin^2\theta}}. \tag{2.7}$$

According to equation 2.7, $d\sigma/d\Omega$ is inversely proportional to the E_0^2. In other words, the beams with higher initial energy have a lower scattering probability for an arbitrary scattering angle, θ. Therefore, the scattering yield decreases with increasing energy. Figure 2.2b compares the differential scattering cross-sections of five different projectiles on a Ru target, calculated by equation 2.7 for the scattering angle of 40°. The change in energy, ranging from 5 keV to 60 keV, reduces the cross-section of each projectile in the plot. Furthermore, different projectiles demonstrate the effect of Z_p (and m_p, which is of the order of $2Z_p$).

Equation 2.7 is obtained using a pure Coulomb potential in which electron screening of the nuclear charges is not included. However, the projectile energies in this study (tens of keV) requires the use of a screened Coulomb potential [1]. Everhart et al. give a scattering cross-sections expression derived from a potential that includes electron screening; that expression exhibits the same energy dependence of E^{-2} as for a pure Coulomb potential.

3 Research Methods

In this section, the research methods used throughout this study are presented. Experimental setup and a simulation program, SRIM, are the two main parts of the section. Experimental setup gives basic knowledge about ECRIS and the beamline, followed by SirPhi and the detectors. The second subsection explains the simulation package SRIM briefly.

3.1 Experimental Setup

This research project was carried out in the research group Quantum Interactions and Structural Dynamics (QISD) at the University of Groningen. The ZERNIKELEIF (Zernike Low-Energy Ion beam Facility) is used for measurements at the QISD laboratory. Figure 3.1 shows the layout of the ZERNIKELEIF. It consists of four main parts: ion source, beam line, CHEOPS and SirPhi, but no experiments are performed with CHEOPS for this study. In this section, the ion source and beamline will be introduced, and then the SirPhi setup with the ESA (electrostatic analyzer) and ToF (time of flight) detectors will be explained in detail.

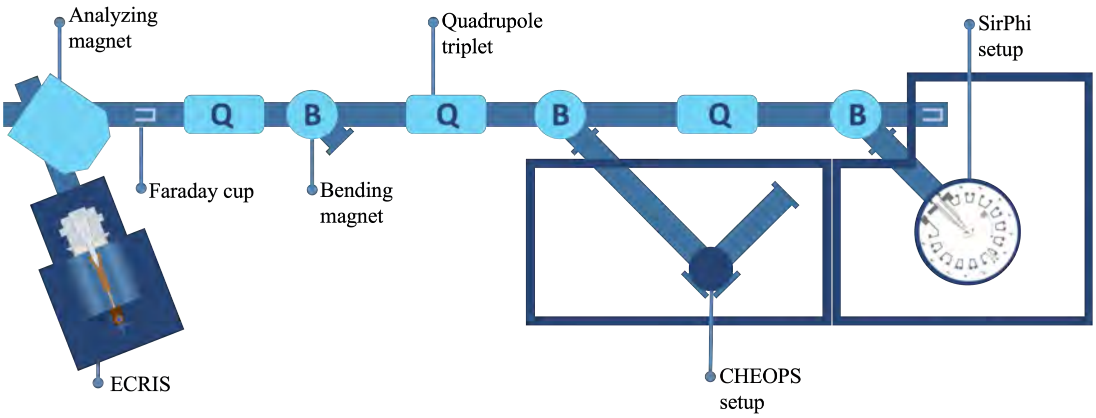

Figure 3.1: A simplified drawing of the ZERNIKELEIF facility including, ion source, beamline, and the CHEOPS and SirPhi setups.

3.1.1 ECRIS and Beamline

The ZERNIKELEIF relies on a plasma source to create multiply charged ion beams. The plasma source is a 14 GHz Electron Cyclotron Resonance Ion Source (ECRIS). It is a supernanogan-type ion source with a copper vacuum chamber in a permanent magnet. The permanent magnet provides a radial and axial increasing magnetic field for plasma confinement and stabilization [9]. The electron Larmor rotation that is enabled by the permanent magnet is resonant with the injected microwaves, and a very efficient heating of the plasma electrons is achieved [10]. The frequency of the electrons gyrating along the magnetic field lines is given by

$$\omega = \frac{e\,|B|}{m_e}. \tag{3.1}$$

To accelerate electrons resonantly, an RF-field with a frequency of 14 GHz is injected via an RF-wave guide (see figure 3.2), which matches the Larmor frequency of electrons at the magnetic surface

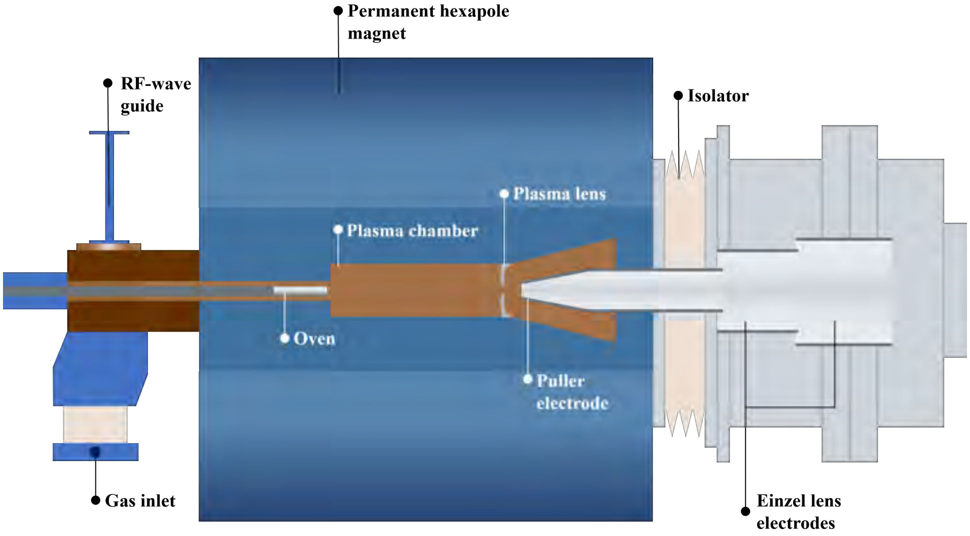

Figure 3.2: A representation of the supernanogan ECRIS. Permanent magnet, plasma chamber, puller and einzel lens electrodes, RF-wave guide, gas inlet, and tin oven are shown.

of 8.6 μT. The process continues with successive ionization of the plasma by the electrons. The gas inlet or the tin oven can be used for providing gas or vapor of the required element (see figure 3.2).

The extraction system gives energy and a certain direction to the ions. The kinetic energy, E_{kin}, of the extracted ions is

$$E_{kin} = q\,(V_{ECRIS} + V_p)\,, \tag{3.2}$$

where V_{ECRIS} is the potential of the source and V_p is the plasma potential. During the experiments subject to this study, a high-voltage power source with a range of 3–20 kV is used. The plasma potential is typically in the range of 10–30 V [1]; therefore, it can be neglected. An electrostatic lens called a puller helps with better extraction. In figure 3.2, einzel electrodes can be seen after the puller. The einzel lens focuses the beam into the analyzing magnet.

Once the ions leave the source, this ion ensemble contains all possible charge states, isotopes, and background gas ionized in the source alongside the desired gas. Therefore, a 110° analyzing magnet (see figure 3.1) is used to select the desired charge state, ion, or isotope. By changing the magnetic field, B_{AM}, the analyzing magnet assures that only the ions possessing a specific mass-to-charge ratio, A/q, can enter the beamline and move further. The trajectories of the ions with other A/q ratios are prevented from entering the beamline. To calculate how much magnetic field is required for a certain A/q ratio, the following formula can be used [3]:

$$B_{AM} = 113.6\sqrt{V_{ECRIS}\frac{A}{q}}, \tag{3.3}$$

where A is the ion mass (in u), V_{ECRIS} is the high-voltage of the source (in kV), B_{AM} is the magnetic field of the analyzing magnet (in gauss) and q is the charge state of the ion. Two important points about the analyzing magnet should be noted. Firstly, the analyzing magnet can adjust only A/q ratio; therefore, beams that have the same A/q ratio cannot be separated. This has to be considered carefully while the results of experiments are being assessed. For instance, $^{120}Sn^{3+}$ and $^{40}Ar^{1+}$ or $^{132}Xe^{3+}$ and CO_2^+ have the same A/q ratio. Secondly, the maximum value of the current source used with the analyzing magnet limits the maximum magnetic field value. The maximum field value for the

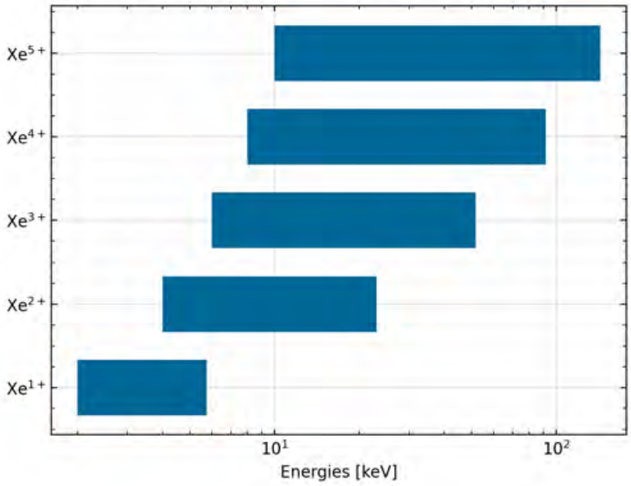

Figure 3.3: Usable energy intervals for Xe ions. The lower limit is determined by extraction and transport efficiency, while the upper limit stems from the maximum value of the magnetic field of the 45° bending magnet in front of the SirPhi setup.

analyzing magnet during the experiments in this study was 4000 gauss because of the current source. This limits the maximum beam energy that can be created for a given A/q ratio.

Just after the analyzing magnet, the ion beam goes through a diaphragm and reaches the first Faraday cup (FC), where the output current of the beam can be measured. When the FC is lowered, the current can be monitored. To transfer the beam further down the beamline, the FC must be raised. Along the rest of the beamline, there are three quadrupole triplet magnets, three bending magnets and, at the end of the beamline, there is another FC that can be used for measuring the transmission ratio. Quadrupole triplets focus the beam to maintain the beam emittance. The last two 45° bending magnets direct the beam to the experimental setups CHEOPS and SirPhi; currently, there is no experimental setup connected to the first 45° bending magnet. The strength of the 45° bending magnet dictates another limit to the experiments; the maximum field value is 3125 gauss for the 45° bending magnet. Hence, this lowers the upper energy limit set by the analyzing magnet. Figure 3.3 shows the possible energy spans that can be realized for the first five positive Xe ions. If there is no deceleration, to compare different energies and charge states, some optimal regions must be chosen. For example, Xe^{1+} can only be compared to Xe^{2+} within the energy range 4–5.5 keV. For Xe^{1+} beams, when the energy of the beam is higher than 5.5 keV, it is not possible to bend it to the experimental setup.

3.1.2 SirPhi

The SirPhi experimental setup is named after “Surface Physics”. It is used for studying ion-surface interactions. The experiments in this work are performed using this setup. It is basically a 300 mm diameter vacuum chamber. The thickness of the chamber walls is 5 mm. In order to prevent stray magnetic fields from entering the chamber, the chamber is made of μ-metal. Also, there are μ-metal shields at the top and bottom parts of the chamber. Once the beam is directed to the SirPhi by the 45° bending magnet, it passes through a differential pumping stage. Before the beam enters the collision chamber, it sees three diaphragms: one just after the bending magnet, and two in front of the deceleration lens system. The collision chamber is kept UHV at $\sim 10^{-10}$ mbar by a 400 l/s ion getter pump. In addition to this, there is a turbomolecular pump for bake-out and initial pumping.

There are three levels to the vacuum chamber: one for experiments and two for surface prepa-

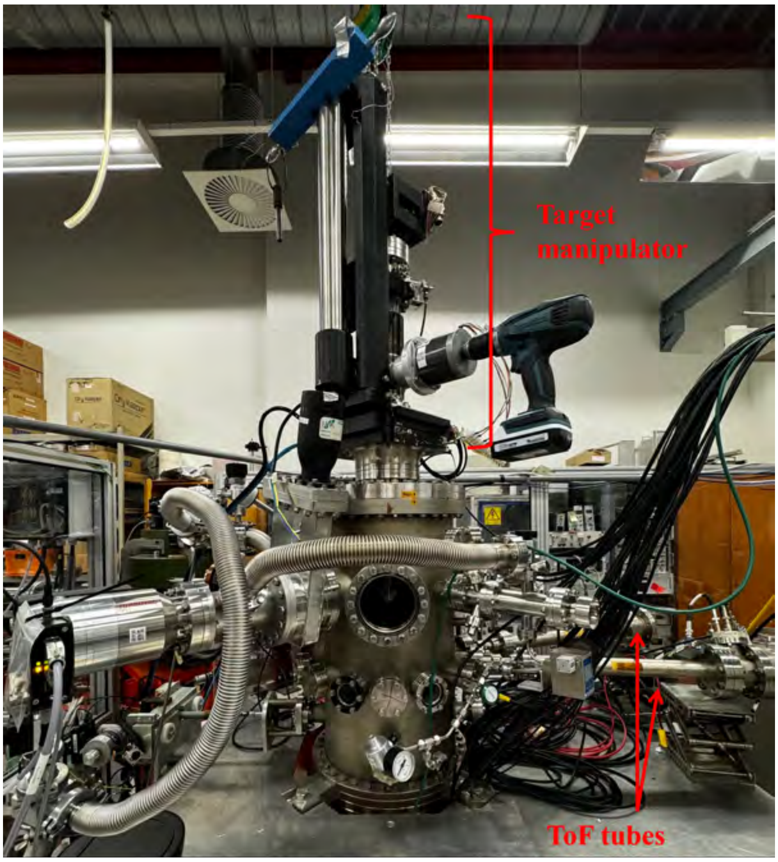

Figure 3.4: An image of the SirPhi setup from outside. The target manipulator and two of the three ToF tubes are indicated.

ration and analysis. The first level of the chamber is for ion-surface interaction experiments and is located at 1400 mm above the ground. Figure 3.5b shows the inside of the collision chamber. The target is attached to the manipulator with a target holder made of two Mo clamps. In figure 3.4, the target manipulator is shown; it has five degrees of freedom. Three of the five are translational: x, y, z, and two are rotational: polar ψ and azimuthal ϕ. The target can be moved in the x and y directions with a range of 25 mm within the plane of the incoming beam, and 400 mm in the z direction, perpendicular to the incoming beam plane. While the manipulator can rotate the target completely around its axis, the azimuthal angle can only be in the range of ± 110. In this study, the azimuthal angle is not changed. The ψ is the angle between the incoming beam direction and the target surface; the θ is the angle in which the detector is placed (see figure 3.5a).

The beam current can be monitored directly on the target or on an FC behind the target. The current measured on the target is recorded to be able to correct for the effect of beam current fluctuations on the results. The correction is made as follows: each count is divided by the recorded current value. Furthermore, when two beams with the same energy and different initial charge states are compared, this correction must be done first by dividing the count by the charge state and then by the corresponding target current. Hence, this quantity specifies the count per particle per target current.

In the experiments, data were collected with two types of detectors: electrostatic analyzer (ESA) and time of flight (ToF) detectors. ESA is inside the collision chamber (see figure 3.5b). It can rotate between the angles (θ) 145° and -115° with respect to the incoming beam. The second type of the detector is the time of flight (ToF) detector. There are three ToF detectors mounted on the collision

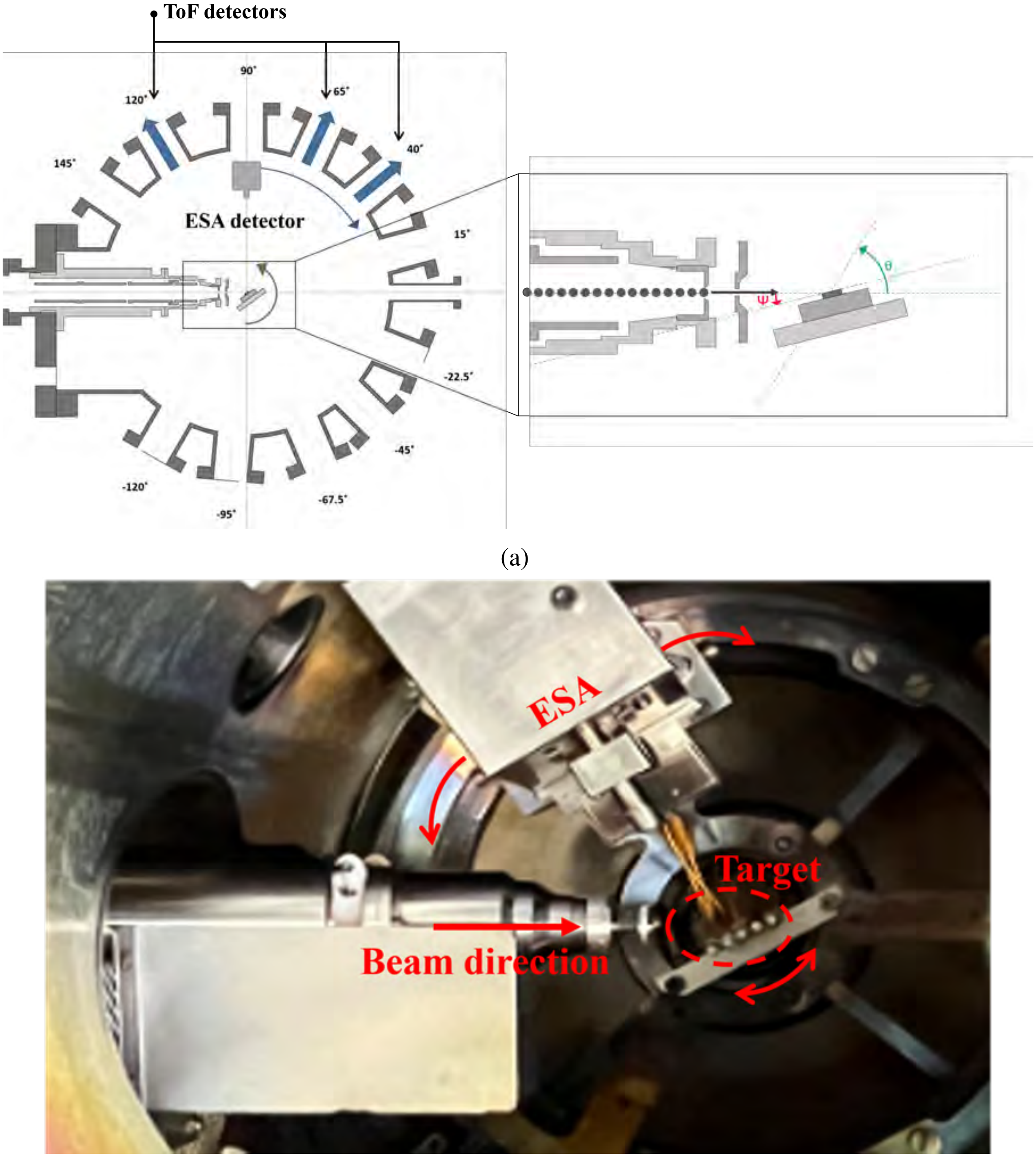

(a)

(b)

Figure 3.5: The illustration of inside SirPhi. The drawing shows the incoming beam, the sample and relevant angles: ψ is the target angle relative to the incoming ion beam; θ is the detector angle relative to the incoming ion beam **(a)**. The image shows the inside of the collision chamber **(b)**.

chamber at the angles (θ) 40°, 65° and 120° with respect to the incoming beam. The positive angles are in the counterclockwise direction; the negative angles are in the clockwise direction (see figure 3.5a).

Electrostatic Analyzer Detector: All energy distributions of reflected and recoiled ions in this study are measured using a 180° semi-hemispherical high-resolution ESA. It can only detect ions;

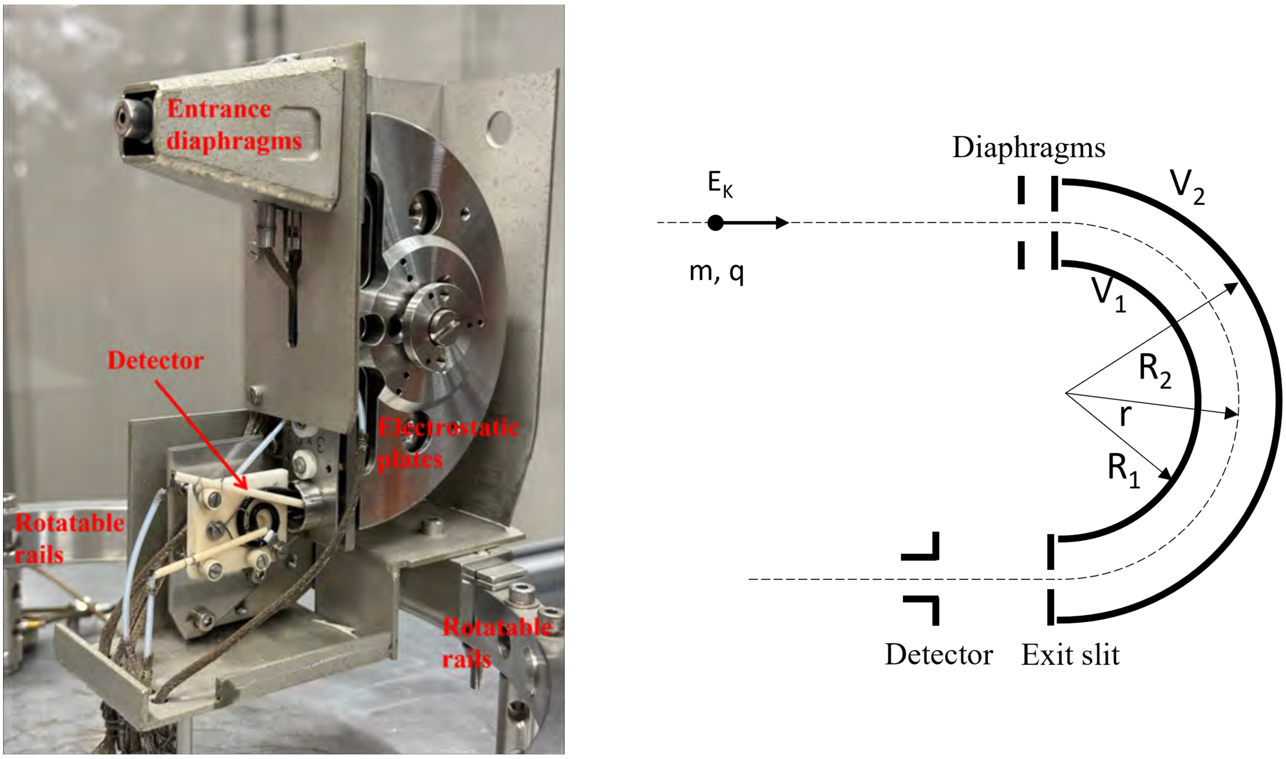

(a) (b)

Figure 3.6: Image of an ESA detector **(a)**. The schematic of the ESA geometry **(b)**.

therefore, ESA spectra contain no information on neutral particles. The reason it is called semi-hemispherical is that the plates are two central slices of hemispheres. Furthermore, it should be noted that the image in the figure 3.6a shows a duplicate of the ESA used in this work; the one used in the measurements in this research has a multichannel plate (MCP) as a detector, not a channeltron.

To explain the working principle of an ESA, it is assumed to be an ideal ESA, which can be seen in the schematic in figure 3.6b. The geometry of the ESA is constructed such that it allows only the ions that have a certain energy to pass through. The energy is determined by the appropriate voltages on the hemispherical plates V_1 and V_2. V_1 and V_2 voltages create an electrical field, E_{ESA}, between the plates. In order for a particle with charge q and mass m to pass through the ESA, it must have a centripetal force, F_{cp}, equal and opposite to the electrical force, F_{ESA} stems from the $\vec{E}_{ESA}$:

$$m\ddot{\vec{r}} = \vec{F}_{cp} + \vec{F}_{ESA} = 0. \tag{3.4}$$

After calculating the $\vec{E}_{ESA}$ between the hemispheres, one obtains the radial equation [11]:

$$\frac{m\dot{r}^2}{r} = \frac{q\left(V_2 - V_1\right)R_1R_2}{\left(R_2 - R_1\right)r^2}, \tag{3.5}$$

where V_1 and R_1 are the electrostatic potential and radius of the inner plate of the ESA; V_2 and R_2 are the electrostatic potential and radius of the outer plate of the ESA; V_r and r are the electrostatic potential and radius of the central trajectory, respectively. A charged particle must have the kinetic energy

$$E_k = q\left(V_2 - V_1\right)F \tag{3.6}$$

to pass the ESA and reach the detector, having the central trajectory r=(R_1+R_2)/2. The coefficient F is called the proportionality factor of the ESA:

$$F = \frac{1}{R_2/R_1 - R_1/R_2}. \tag{3.7}$$

Furthermore, to be sure that the particle is not accelerated or slowed down by the $\vec{E}_{ESA}$ inside the ESA channel, V_1 and V_2 must be selected such that V_r is zero. If V_2/V_1=-R_1/R_2, then the condition is satisfied and V_r is zero for an ideal hemispherical ESA. The ESA used in the experiments has R_1=48 and R_2=52 mm, which give V_2/V_1=-0.923 and F=6.24. However, the ESA used in the experiments is not an ideal but a semi-hemispherical ESA. From calibration, it is reported that V_2/V_1=-0.935 and F=6.42 [12]. Once the exit slit is passed, the particles are detected by a multichannel plate (MCP). Data acquisition electronics count the MCP signals. The electrical potentials on the plates of the ESA can be regulated by a homemade Labview program.

The energy specified by the plate voltages is basically the quantity E_k/q. It is defined as E_{pass}, and the ESA spectra throughout this work are presented with E_{pass}. For example, an ion possessing a kinetic energy of 4 keV with the charge state 1+ has the E_{pass} value of 4 keV in the spectrum. On the other hand, an ion with E_k=8 keV and q=2+ will also pass E_{pass}=4 keV in the spectrum. These two particles are detected with the same V_1 and V_2 combination (see Eq. 3.6). Another important point connected to the data representation of this study is the energy resolution correction. The energy resolution of the ESA (ΔE/E) is determined by the diameters of the diaphragms, the radius of the ESA, and the angular divergence of the beam [1]; this implies that the ratio, ΔE/E, is constant. Because of this energy resolution feature of the ESA, the raw counts are divided by the energy as a second correction in addition to the target current correction. Thus, the counts on the ESA spectra have the unit eV^{-1} in addition to the previous correction due to the target current.

For a proper backscattering energy spectrum, the yield must also be corrected for the ion detection efficiency. Although, the ion detection efficiency of an MCP depends on the kinetic energy of the ion, the detection efficiencies are not simply a function of the impact velocity or the impact energy. Rather, for an MCP, the efficiencies scale to a single curve when plotted as a function of the impact energy divided by the square root of the ion mass [13]. In this study, following Krems et al., the polynomial fitting equation

$$\log\eta = -0.257 + 0.161x - 0.239x^2 - 0.0184x^3 - 0.3x^4, \tag{3.8}$$

where η is the detection efficiency and x=log($E_k/\sqrt{m}$), is used for detection efficiency correction of the MCP.

Time of Flight Detectors: The experimental setup has three ToF tubes, mounted at angles 40°, 65° and 120° with respect to the incoming beam direction. ToF detectors give a time spectrum of the reflected and recoiled particles. Unlike ESA, ToF can detect both charged and neutral particles. To construct a time spectrum, the continuous beam should be converted to a pulsed beam. Therefore, there is a chopper-sweeper system between the 45° bending magnet and the deceleration lenses. In figure 3.7, a diagram of a chopper-sweeper system is presented. It consists of two pairs of parallel plates. When the chopper plates are at equal and opposite voltages, ±V*chopper*, the beam bends because of a force caused by the electric field between them. As a result, it is intercepted and fails to traverse the exit diaphragm. The field changes direction, and the beam bends, but this time in the opposite direction, when the potentials on the plates change polarity. Hence, the beam sweeps the exit diaphragm, and the pulsed beam is produced. To ensure proper time resolution, pulses from the positive flank can be deflected by the sweeper plates.

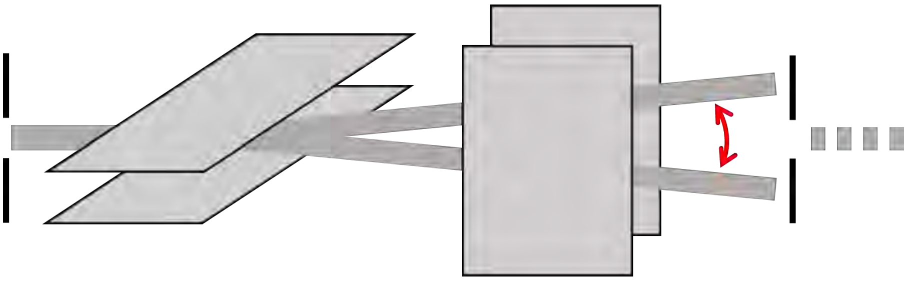

Figure 3.7: Schematic diagram of a chopper-sweeper system.

Each ToF tube on the experimental setup comprises a stainless steel outer tube that is encased within an isolated inner tube. At the end of the inner tube, a channeltron detector is located. After a collision event, the reflected or recoiled particles travel 577 mm from the target to the detector. The sweeper sets the beginning of the pulsed beam, and the detector marks the end of flight; Thus, a time spectrum is constructed. If it is desired to separate charged particles from neutral ones, voltage can be applied to the inner tube, thereby accelerating the ions toward the detector or decelerating them. However, no experiment, in this study, is performed by biasing the inner tube.

3.2 Simulation Program: SRIM

In this thesis, the simulations were conducted by using a software package called SRIM (Stopping Range In Matter). Originally, the package was developed to calculate stopping power tables, mainly for high-energy ions where electronic stopping power is dominant [14, 15]. Later on, a new module was added to SRIM. This addition is called TRIM (Transport of Ions in Matter), in which interactions between atoms and targets can be simulated. It is a Monte Carlo simulation that uses ZBL potential as a screening potential. A backscattering energy distribution can be created for a certain detection angle, θ, since TRIM can calculate the energy and the exit angle of atoms leaving the target.

Each projectile is created one by one at the edge of the target. The positions of successive collisions are determined by the mean free path length. The collision events are treated as binary collisions. An impact parameter is determined randomly for each collision. A scattering angle and energy loss are calculated using that impact parameter. For the next collision, the calculated scattering angle and mean free path are checked. If the position of the next collision is above the surface, the energy, direction, and coordinates of the projectile are saved to the output file by considering this projectile as backscattered. If the position of the next collision is inside the target, the projectile either continues to the next collision or is recorded as stopped, depending on its kinetic energy.

The data of backscattering spectra is written in the BACKSCAT.txt file. In addition to energy and position data, direction is given by the cosine of the angles with respect to the x, y and z axes. In the notation of the program, α, β and γ are the angles regarding the x, y and z axes, respectively. Figure 3.8 illustrates the coordinate system and corresponding angles used by SRIM. The x—axis is perpendicular to the surface; the positive direction is pointed into the target when the entrance point is taken as the origin. The y—axis is along the target surface. Since incoming ion direction and reflected or sputtered particle directions are in the same plane in the experimental setup, the results only with $\cos\gamma = 0$ are used in the simulations. Figure 3.8 shows the xy-plane with the angles we used in the experimental setup. While we define the incidence angle of an ion with respect to the surface, the program defines the incidence angle regarding the surface normal. Therefore, if you want to simulate a beam with an incidence angle of 15 degrees according to the experimental setup, $90 - \psi = 75°$ should be given to the program as the incidence angle parameter. Furthermore, to

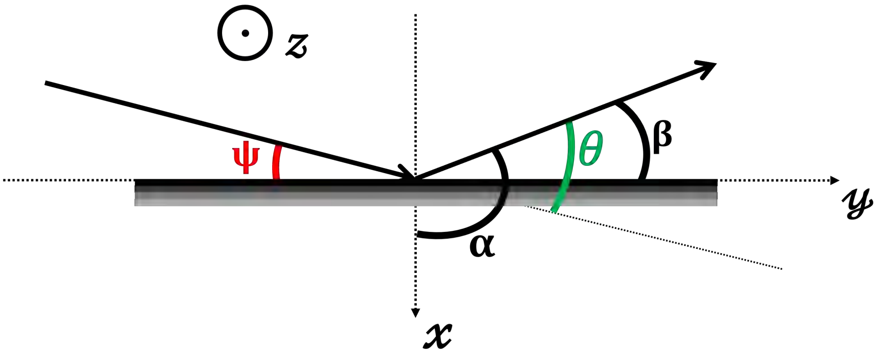

Figure 3.8: The coordinate system of SRIM and corresponding angles.

calculate the detection angle, θ, from the geometry of the program, we can write

$$cos\theta = sin\psi cos\alpha + cos\psi cos\beta. \tag{3.9}$$

From the data in the BACKSCAT.txt of a simulated beam with a predefined energy and an incident angle, a backscattering energy spectrum for a certain detection angle, θ, can be obtained by using Eq. 3.9. However, it should be kept in mind that the program does not take into account charge-state-related effects. Therefore, a backscattering energy distribution obtained from ESA, which only detects ions, may differ from the simulated backscattering spectra if the ionization fraction varies over the energy range of detected ions. Moreover, the BACKSCAT.txt file does not contain primary recoils. Hence, a spectrum emulated using this file will not show recoiled particles.

4 Results and Discussions

In this section, the results of the Xe measurements are presented. The measurements are taken using ESA and ToF detectors, which were already explained in detail in Chapter 3. The experiments are performed with six different beams: 5 keV Xe^{1+}, 15 keV Xe^{3+}, 20 keV Xe^{2+}, 45 keV Xe^{3+}, 45 keV Xe^{4+}, and 60 keV Xe^{4+}. ESA measurements are taken at the angles 20°, 30°, 40°, and 50°, while ToF measurements are done at the angles 40°, 65° and 120°. Moreover, 15 keV Xe^{2+} and 33.75 keV Xe^{3+} beam measurement data are used with permission of L. Assink [5]. Firstly, ESA results are given and discussed, focusing on three different aspects: initial energies, initial charge states and overall energy distribution. Then, the data obtained from ToF is given, followed by SRIM results. In all spectra shown in this chapter, the following color code is used: red and blue bars show the energy intervals where the SC and (S)DC peaks are expected. A green bar is used to indicate the position of the recoil (REC) peak. The bars have different widths because of the natural abundance of Ru.

4.1 Initial Energy

In figure 4.1, one can see the ion scattering spectra of 15 keV and 20 keV Xe^{2+} beams on a Ru target at the incident angle of $\psi = 15°$ and the detection angle of $\theta = 40°$.

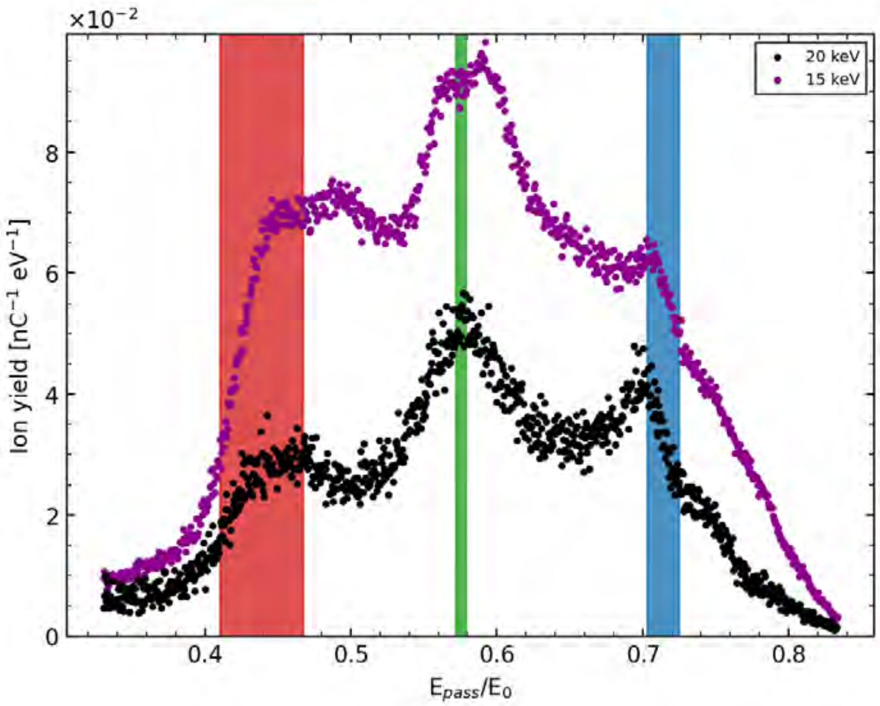

Figure 4.1: The energy distribution of the reflected and recoiled ions of 15 and 20 keV Xe^{2+} beams on a Ru target over an incident angle of ψ=15° and detection angle of θ=40°.

According to the equation 2.4, the SC peak of the 15 keV Xe^{2+} beam is expected around $0.45E_0$. Moreover, detection over the angle of 40° gives DC combinations, e.g., 15-25, 10-30, etc., with a maximum limit of $0.72E_0$ for SDC. From the 15 keV Xe^{2+} spectrum (see figure 4.1, magenta dots), it can be seen that there is a bend corresponding to the expected SC region rather than a clear peak. A ridge can be considered as a DC peak coinciding with the blue-lined interval. On the other hand, an evident peak sits around $0.58E_0$, where the recoil peak is expected (Eq. 2.6). The intensity of this

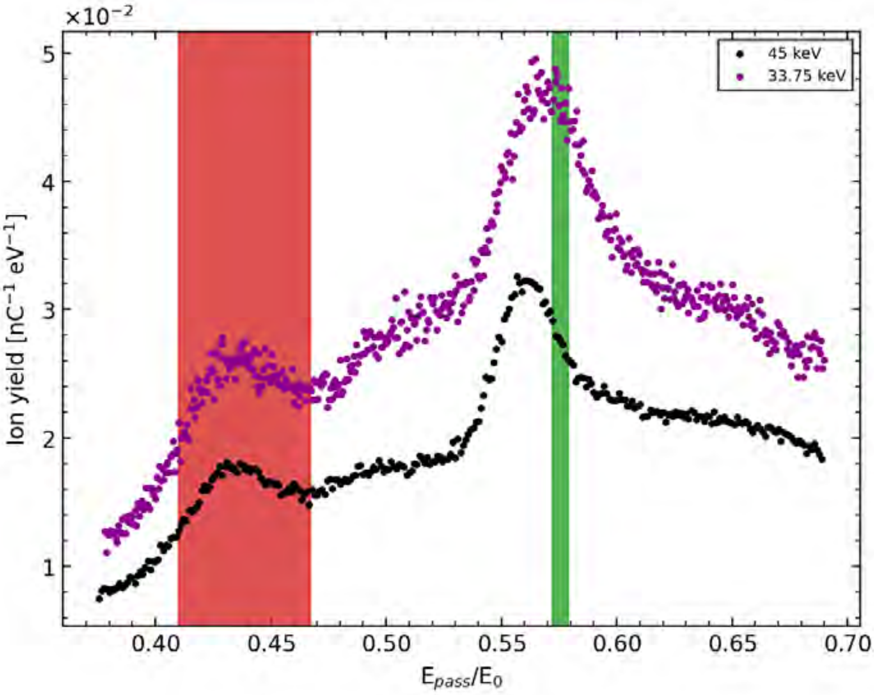

Figure 4.2: The energy distribution of the reflected and recoiled ions of 33.75 and 45 keV Xe^{3+} beams on a Ru target over an incident angle ψ=15° and detection angle θ=40°.

recoil peak is just above 0.08 $nC^{-1}eV^{-1}$, while the SC and DC peaks are around 0.05 $nC^{-1}eV^{-1}$. The black dots in figure 4.1 represent the backscattering energy distribution of a 20 keV Xe^{2+} beam on a Ru target for the same scattering geometry. Although the peaks are at higher energies for the 20 keV Xe^{2+} beam, they correspond to the same E_f/E_0 and E_{rec}/E_0 ratios. From the energy distribution of the 20 keV Xe^{2+} beam, the prominent REC and DC peaks can be seen with intensities of 0.056 $nC^{-1}eV^{-1}$ and 0.049 $nC^{-1}eV^{-1}$, respectively. As for the SC peak, there is a small peak with an intensity just above 0.035 $nC^{-1}eV^{-1}$ within the red bar.

As the energy of the incoming beam changes from 15 keV to 20 keV, the overall counts and intensities of the SC, DC, and REC peaks decrease. Equation 2.7 guarantees lower differential scattering cross-section because of E_0^{-2} dependence. Since the energy ratios of these beams are 3/4, their differential scattering cross-section ratio should be 9/16, which is approximately 1/2. This leads to less backscattering probability for the 20 keV beam, thereby yielding a count that is almost half of the 15 keV beam. Moreover, the Xe^{2+} ions in the 20 keV beam can penetrate further into the target and experience a higher amount of deeper layer interactions compared to the ions in the 15 keV beam. The ion beam with higher energy creates fewer on- and near-surface events but more deeper-layer interactions because of further penetration. Hence, higher energy results in a significant decrease in count.

In figure 4.2, we present another comparison between the beams with different initial energies but the same initial charge state: 33.75 keV Xe^{3+} and 45 keV Xe^{3+} beams on a Ru target with the same scattering geometry as before. In the scattering spectrum of the 33.75 keV Xe^{3+} beam (the magenta dots in the figure 4.2), there is a visible peak with the intensity of 0.028 $nC^{-1}eV^{-1}$ within the expected SC interval. The REC peak of this beam has an intensity of 0.05 $nC^{-1}eV^{-1}$.

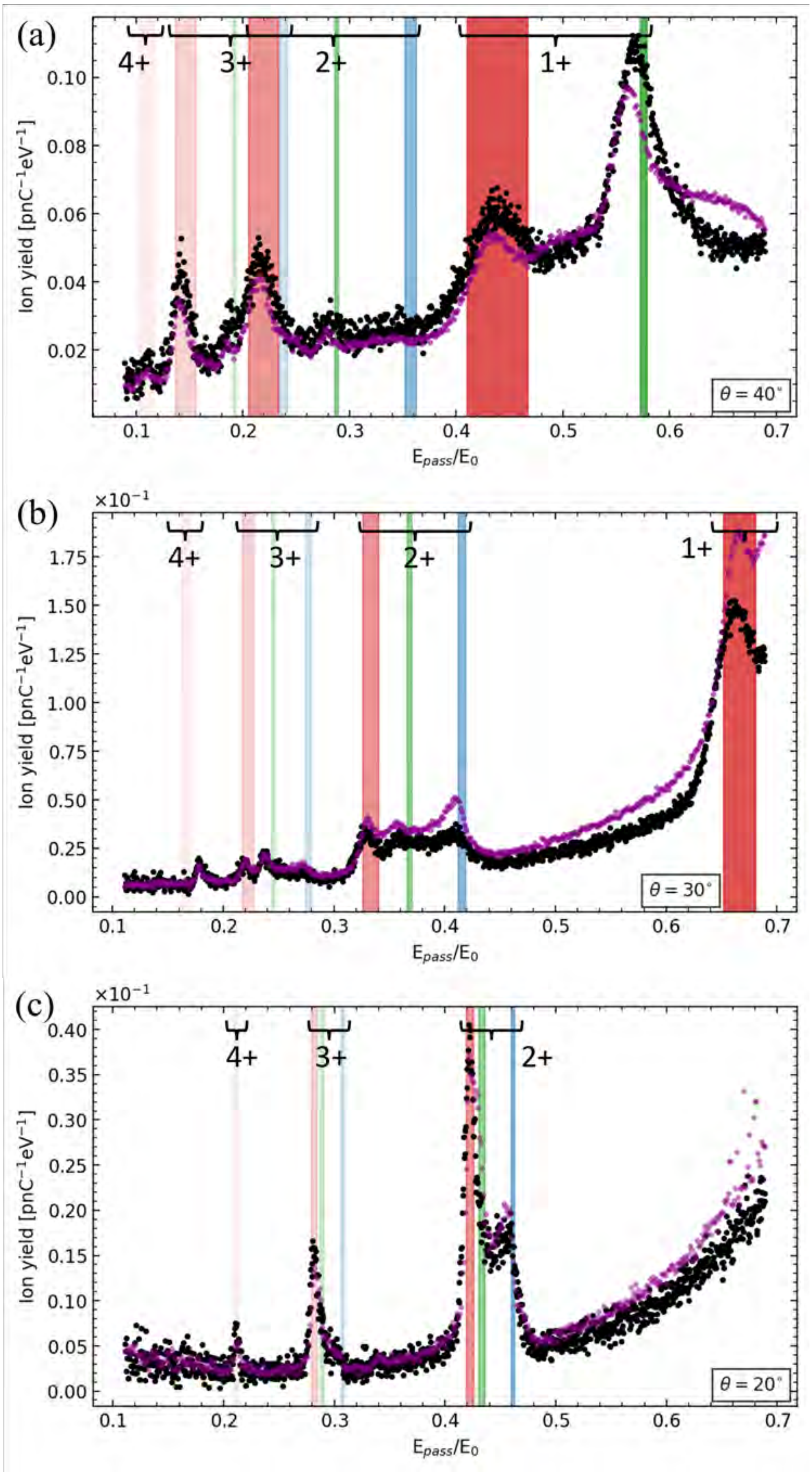

Figure 4.3: The scattering spectra of 45 keV Xe^{3+} (dark magenta) and Xe^{4+} (black) at the target angle ψ=15° and the detection angle **(a)** θ=40°, **(b)** θ=30° and **(c)** θ=20°.

The energy distribution of the 45 keV Xe^{3+} beam is plotted with black dots in Fig. 4.2. The estimated SC region corresponds to a peak with an ion yield intensity of 0.018 $nC^{-1}eV^{-1}$ for the spectrum of this beam. Another peak of the spectrum has an intensity of 0.031 $nC^{-1}eV^{-1}$, but the maximum of this peak occurs just before the theoretical value range of the recoil energy value.

Consistent with the previous result, figure 4.2 shows a lower count for the beam with higher energy. Increasing beam energy can increase the penetration depth of the projectiles into the target and may cause more interaction at deeper layers. Furthermore, higher initial energy reduces scattering cross-section and, thereby, scattering probability. These can be possible explanations for fewer counts for higher energy. On the other hand, increasing energy does not change the shape of the spectra for Xe^{3+} in figure 4.2, unlike in figure 4.1 for Xe^{2+} where the spectral shapes change somewhat. Furthermore, the experimental REC peak seems to shift to lower energies with increasing initial energies.

4.2 Initial Charge State

To evaluate the effect of the initial charge state on the energy distributions of reflected and recoiled ions, two beams with the same initial energy, but different charge states are compared. In figure 4.3, the energy distribution of 45 keV Xe^{3+} and 45 keV Xe^{4+} are illustrated at the incident angle of $\psi = 15°$ and the detection angles of $\theta = 40°$, $\theta = 30°$, and $\theta = 20°$. It should be noted that the counts of the spectra are also corrected as per "particle" by dividing the accumulated charge by the charge state of the ions (pnC^{-1}), unlike the comparison in the previous subsection. After collision events, reflected and recoiled ions can end up with different charge states. In other words, an SC event can yield, with changing probabilities, neutral Xe, Xe^{1+} or Xe^{2+} and so on; similarly, a recoiled Ru can be neutral or charged with different states; only probabilities are different for ending up with different charge states. Therefore, increasing the transparency of stripe colors in figure 4.3 indicates the SC, DC, and REC peaks of the higher charge states, while the meanings of the stripe colors remain the same. For example, the darkest red stripe indicates the SC energy interval of backscattered Xe^{1+} ions. As the color of the stripe gets more transparent, it marks higher charge states for backscattered or recoiled ions, e.g., Xe^{2+}, Xe^{3+} or Ru^{2+}, Ru^{3+} etc. The ions that have different charge states are detected at different pass energies, E_{pass}, by the ESA detector.

Figure 4.3a shows the backscattering spectra of 45 keV Xe^{3+} and Xe^{4+} beams over a detection angle of $\theta = 40°$. Since the spectrum of the Xe^{4+} beam is relatively noisy, an exact comparison of the intensity of these beams cannot be done quantitatively. Nevertheless, there is no significant difference between the total number of counts for each of the beams. Likewise, the spectral shape within the energy interval subject to figure 4.3a is almost the same. For a detection angle of $\theta = 30°$ (see figure 4.3b), the high-energy part of the spectrum of the Xe^{3+} beam has a higher number of counts than the Xe^{4+} beam; there is a difference of 0.025 $pnC^{-1}eV^{-1}$ between the SC peaks of the beams. However, the overall shape of the spectra are quite similar, as shown in figure 4.3a. In figure 4.3c, the plot of the beams demonstrates a perfect match between the spectral shapes of the Xe^{3+} and Xe^{4+}.

Although different detection angles change the spectral shape as a whole, this seems to alter the spectra in a very similar way. For the same detection angle, the spectral differences between the beams Xe^{3+} and Xe^{4+} are so small that they may stem from taking the measurements on different days. The resulting energy distributions of the beams with the same initial energies do not seem to be affected by having different charge states initially.

As a further step, the spectra of all the beams can be compared, regardless of their initial charge states and energies. Fig. 4.4 shows the compilation of all the beams (15 keV Xe^{2+}, 20 keV Xe^{2+}, 33.75 keV Xe^{3+}, 45 keV Xe^{3+}, and 45 keV Xe^{4+}) in one plot with normalized yield on the y-axis.

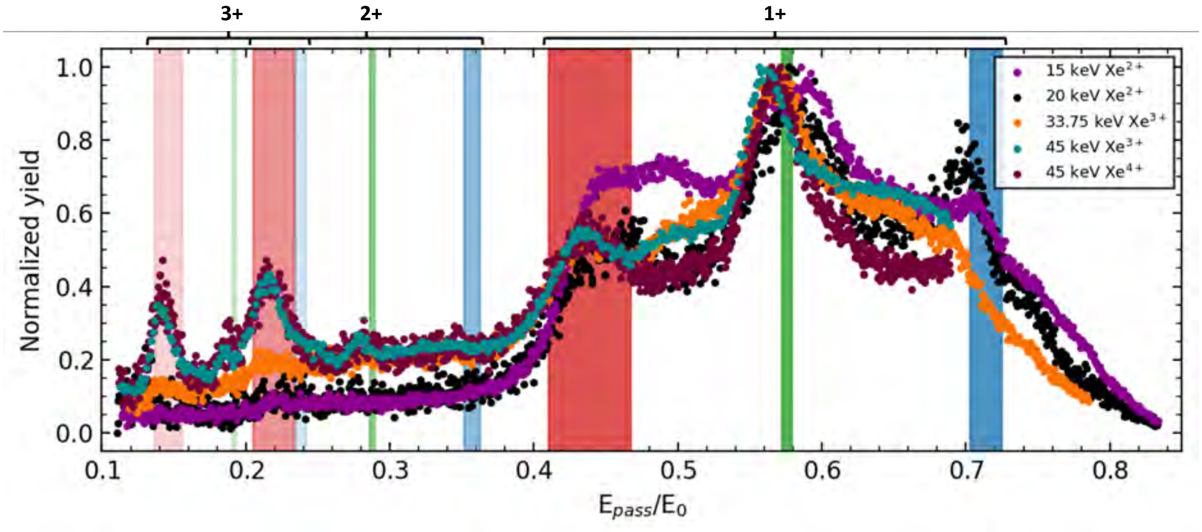

Figure 4.4: The whole scattering spectra ($0.1E_0$—$0.83E_0$) of 15 keV Xe^{2+}, 20 keV Xe^{2+}, 33.75 keV Xe^{3+}, 45keV Xe^{3+}, and 45 keV Xe^{4+} on the Ru surface at target angle $\psi = 15°$ and the detection angle $\theta = 40°$. More transparent stripes indicate backscattered and recoiled particles with higher charges. The darkest ones are 1+, and the most transparent ones are 3+.

For the beams with higher initial energies, the recoil peak is shifted a bit to lower energies. Unlike the recoil peaks, the SC peaks do not show shifting behavior with changing energy. It is hard to say something about DC peaks because the DC region of the 45 keV beams exceeds the maximum ESA detection energy.

Another notable feature of the spectrum in Fig. 4.4 is the bumps before and after the REC peaks of the 33.75 and 45 keV Xe^{3+} beams. These bumps appear in the spectra of the 33.75 and 45 keV Xe^{3+} beams and match in shape. Moreover, they are the only difference between the 45 keV Xe^{3+} and Xe^{4+} beams. Therefore, the reason behind these bumps appears to be the initial charge state of Xe^{3+} beams. They can stem from a mixed beam effect; a background gas that has the same A/q ratio with Xe^{3+} can be selected by the analyzing magnet alongside the Xe^{3+} ions. Such a second beam alongside Xe^{3+} might explain these bumps, which do not exist in the spectra of 15 keV, 20 keV Xe^{2+} and 45 keV Xe^{4+}.

There are two peaks at the low-energy part of the spectra of 45 keV Xe^{3+} and Xe^{4+}. These are the SC peaks that stem from the reflected ions keeping higher charge states: the most transparent red bar is the SC peak caused by the reflected Xe^{3+} ions; the less transparent red band in the middle is the SC peak originating from the reflected Xe^{2+} ion. However, the spectra of the other beams (33.75 keV, 20 keV and 15 keV) have the SC peak only from Xe^{1+} particles. A possible reason why only 45 keV beams have 2+ and 3+ SC peaks may be their higher initial energy. Having a higher initial energy, such as 45 keV here, seems to make it more probable for highly charged particles to maintain their charge until they reach the detector. In other words, projectiles with higher energies do not have enough time to complete their neutralization on their way toward or away from the surface. Varying initial charge states should also have an effect on charge exchange channels due to changing ionization energies, but it is not possible to make a statement about it from backscattering spectra. Another important point about the higher charge state peaks is the absence or weakness of the recoil peak with charges greater than 1+ due to the low probability of further ionization of recoiled Ru ions. This situation can provide a better comparison of the simulations to the experimental spectra because SRIM does not consider the recoiled particles in its resulting spectra.

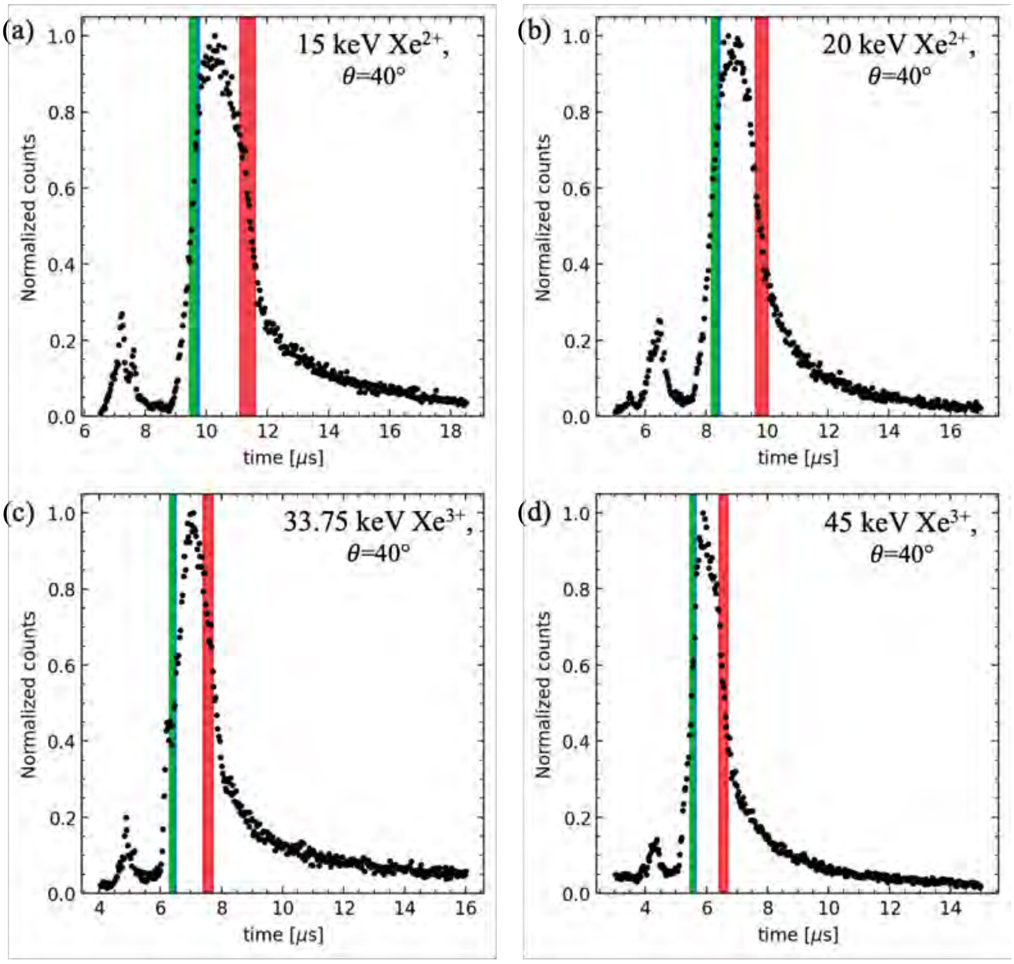

Figure 4.5: ToF spectra of 15 **(a)** and 20 **(b)** keV Xe^{2+} beams, and 33.75 **(c)** keV and 45 **(d)** keV Xe^{3+} beams taken at a detection angle of 40° and incident on the Ru sample at an angle of 15°. The positions of SC, DC, and REC peaks are converted from their energy values. The DC and REC peaks (blue and green) overlap.

4.3 Time of Flight Results

Figure 4.5 shows the energy distributions of reflected and recoiled particles belonging to 15 and 20 keV Xe^{2+} beams, and 33.75 keV and 45 keV Xe^{3+} beams obtained from the ToF detector mounted at an angle of 40°. ToF measurements contain reflected and recoiled atoms in addition to ions. Therefore, it is not possible to see distinct SC, SDC or REC peaks in the ToF spectra, unlike the ESA spectra. Nevertheless, there is a feature that is common for every spectra in figure 4.5; it is the surface contamination peaks showing up at short flight times. The flight times of a recoiled C and O atom correspond to these peaks. However, they create a single contamination peak since their corresponding flight times are so close, except for the 15 keV Xe^{2+} beam, which are 6.5 and 6.4 μs for O and C, respectively. For the projectiles with higher energies, a higher sputter yield is expected; therefore, the spectrum of higher-energy beams should have more contamination counts than the beams with lower energies. In figure 4.5, however, the spectra of the beams with higher energies have fewer contamination counts relative to their maximum counts. The lower backscattering probability for higher initial energy and fewer first-layer interactions, despite the increase in the sputter yield, might be possible reasons for the decrease in the intensity of these contamination peaks.

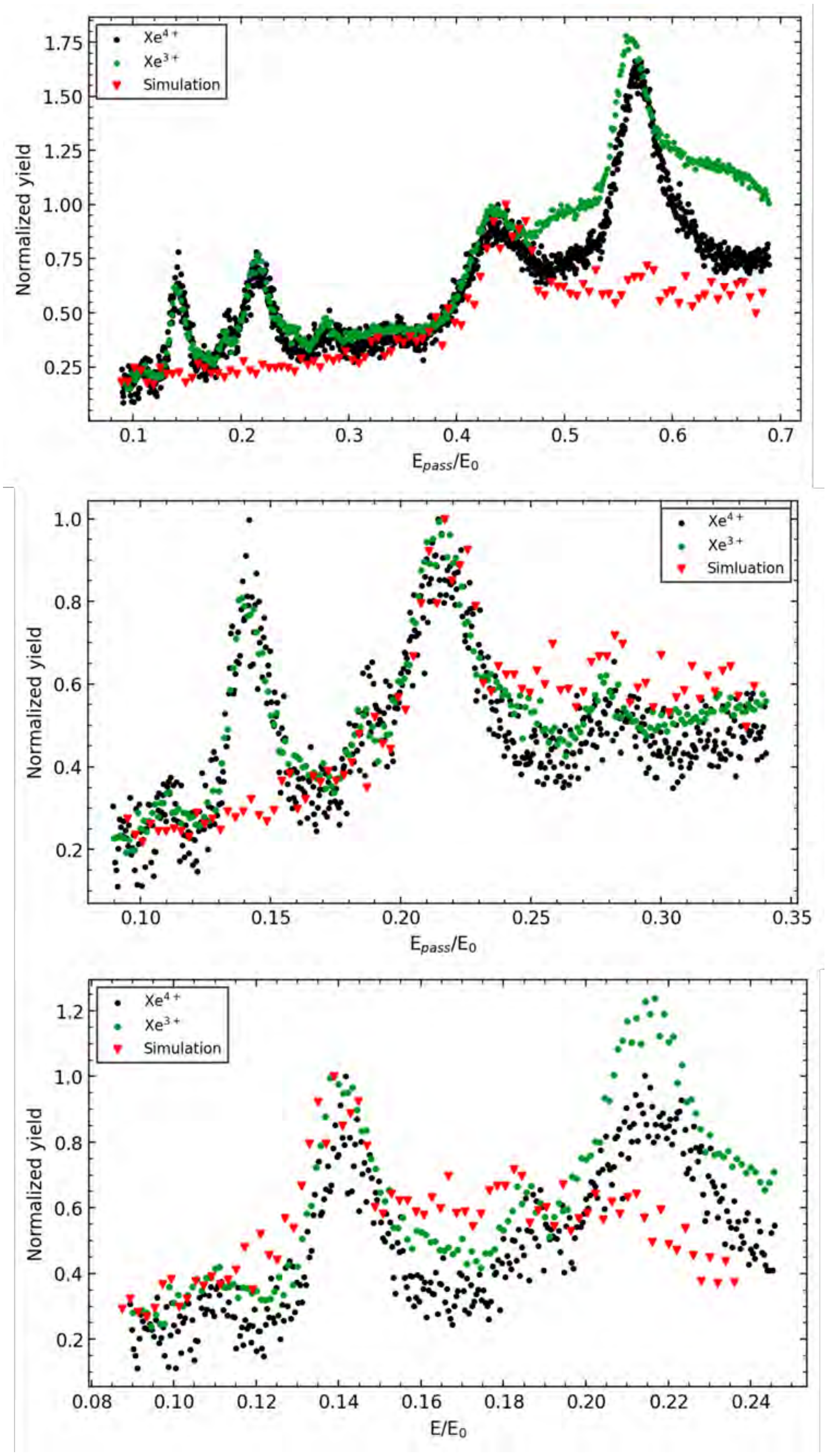

Figure 4.6: Comparison of an SRIM simulated spectrum (45 keV Xe (orange)) to the full experimental spectra (green and black) **(a)**. Panels **(b)** and **(c)** show zoom-ins into the 2+ and 3+ energy ranges. The SRIM energies in the spectrum are scaled by 1/2 and 1/3 to match 2+ and 3+ SC peaks of experimental spectra.

4.4 Simulations vs. Experiments

To compare experimental and simulated spectra, two simulations are performed for a 45 keV Xe beam at the incident angle ψ=15° by using SRIM and combined for higher statistics. Figure 4.6 shows overlapped backscattering spectra of 45 keV Xe^{3+} and Xe^{4+} beams, and the simulated spectrum of a 45 keV Xe beam. Figure 4.6a is created by normalizing the spectra to their SC peaks. Considering that SRIM does not take into account charge states and recoiled particles, the SC peak shapes of all three spectra have a good match. Moreover, the height of SC to background ratio similarity is significant, except for the bumps before and after the recoil peak of the Xe^{3+} beam. Since the Xe^{4+} beam has a better match than the Xe^{3+} beam with simulation shape, the previous argument on the probability of having a second beam alongside the Xe^{3+} beams becomes stronger with this observation.

Figures 4.6b and 4.6c illustrate the overlaps of the simulation spectrum with the SC peaks of reflected Xe^{2+} and Xe^{3+} ions at the lower energy part of the experimental spectra. Since the ionization probability for becoming 2+ and 3+ for Ru is low, Ru^{2+} and Ru^{3+} recoil peaks are not clearly observed above the background. Therefore, having a good shape match in this part of the spectra with the simulated spectrum is expected. In figure 4.6b, the SC peaks caused by reflected Xe^{2+} of both beams and the simulated spectrum scaled by 1/2 are put on top of each other. The overall shape and width of the peaks are in good agreement.

In figure 4.6c, the simulated spectrum scaled by 1/3 and the SC peaks caused by reflected Xe^{3+} ions of both beams are compared this time. Even though the widths of experimental 3+ SC peaks and simulated SC peak show a fairly good match, the overall spectral shapes around the experimental 3+ SC peaks differ from the SRIM simulated spectra. Experimental spectra have a lower background than simulated spectra with respect to corresponding peak maxima.

5 Conclusions

To gain a more profound understanding of the interactions of heavy, low-energy ions with surfaces, it is important to explain the absence of the SC peak observed in previous studies for Sn ions on transition metal surfaces, e.g., Ru and Mo. In this thesis, it is aimed to see whether the SC peak can be observed for another projectile, Xe, which is heavier than the target atom similar to Sn, and to test the predictions of BCA.

For the same charge states, changing initial energies were studied. Unlike Sn experiments, SC peaks were observed in the energy distributions of scattered Xe ions, though they are low in intensity compared to lighter projectile—heavy target experiments. Another important result is that increasing beam energy yields a lower overall number of counts. The peaks associated with the recoils are dominant in the spectrum of all beams with varying energies. In another set of experiments, Xe beams with the same initial energy, but different initial charge states were used. These experiments have demonstrated that the initial charge state does not have a substantial influence on the shape and intensity of the resulting energy distribution. When all spectra are compared regardless of their initial energy and charge states, the ions with higher initial energy, such as 45 keV here, may not complete their neutralization creating SC peaks for higher charge states in ESA spectra. ToF results do not indicate a clear result about interactions since they contain both charged and neutral reflected and recoiled particles and do not have distinct SC, DC, or REC peaks. However, these results provide some information about surface contamination. As for the SRIM simulation, Xe ion beam simulations are generally in good agreement, although SRIM simulated spectra do not contain recoils and charge effects. On the other hand, the absence of recoils and charge state effects in SRIM spectra can be used for comparisons to SC peaks stemmed from highly charged reflected projectiles in experimental spectra.

To generalize and refine the results obtained here, more experiments with different energies and charge states must be done. As these experiments are compared to corresponding simulation results, simulation packages can be improved further. Furthermore, the possibility of replacing the Ru target with a different heavier material, a material heavier than Xe, e.g., W or Au, could be insightful.

Bibliography

[1] M. Deuzeman, *Generation and interactions of energetic tin ions*. PhD thesis, 2019.

[2] V. Y. Banine, K. N. Koshelev, and G. H. P. M. Swinkels, "Physical processes in euv sources for microlithography," *Journal of Physics D: Applied Physics*, vol. 44, p. 253001, jun 2011.

[3] S. Rai, *Ionic interactions around EUV generating tin plasma*. PhD thesis, 2023.

[4] S. Rai, K. I. Bijlsma, S. Koeleman, O. G. Tjepkema, A. W. Noordam, H. T. Jonkman, O. O. Versolato, and R. Hoekstra, "Single-collision scattering of kev-energy kr ions off a polycrystalline cu surface," *Nuclear Instruments and Methods in Physics Research, Section B: Beam Interactions with Materials and Atoms*, vol. 482, pp. 58–63, 11 2020.

[5] L. A. et. al., "in preparation," 2024.

[6] W. K. Chu, J. W. Mayer, and M. A. Nicolet, *Backscattering Spectrometry*. Academic Press, Inc, 1987.

[7] W. Möller, "Fundamentals of ion-solid interaction - a compact introduction," wissenschaftlich-technischer bericht / hzdr, 2017.

[8] H. Goldstein, C. Poole, J. Safko, and S. R. Addison, *Classical Mechanics, 3rd ed.* Addison Wesley, 2001.

[9] R. Goldston, *Introduction to Plasma Physics*. CRC Press, 2020.

[10] S. Saminathan, *Extraction and transport of ion beams from an ECR ion source*. PhD thesis, 2011. Relation: http://www.rug.nl/ Rights: University of Groningen.

[11] D. Winters, *Polarization transfer in ion-surface scattering*. PhD thesis, 2004.

[12] L. Folkerts, *Charge exchange of multiply charged ions with metal surfaces*. PhD thesis, 1992.

[13] "Channel electron multiplier and channelplate efficiencies for detecting positive ions," *Review of Scientific Instruments*, vol. 76, 9 2005.

[14] J. F. Ziegler, J. P. Biersack, and U. Littmark, "stopping and range of ions in solids," 1985.

[15] J. F. Ziegler, M. Ziegler, and J. Biersack, "Srim – the stopping and range of ions in matter (2010)," *Nuclear Instruments and Methods in Physics Research Section B: Beam Interactions with Materials and Atoms*, vol. 268, no. 11, pp. 1818–1823, 2010. 19th International Conference on Ion Beam Analysis.

Acknowledgments

Foremost, I would like to express my deepest gratitude to Ronnie Hoekstra for providing me with this master research project. I am amazed at how much I have learned and improved. I also want to thank you for being such nice and kind to us. Further, I would like to thank to Antonija Grubisic-Cabo for willing to be second examiner of my project.

Luc, I do not know how to thank you sufficiently for your guidance, supervision, and patience. You have helped me a lot to overcome my hesitations and fear of failure; thank you very much! I would like to thank everyone in the QISD/Ion Interactions group, Klaas, Mart, Emiel, Denisse, Michiel, Lennart, Symen, Matthijs, Thomas and Harry, for the wonderful time I spent during my research. Thanks to you all, I have seen how amazing it can be to work with such a nice and talented group.

Appendix

In this appendix, we present all the plots that belong to the beams we performed in experiments during this research project. Thus, the reader can see the results that we did not include in the body of this thesis because of insufficient statistics.

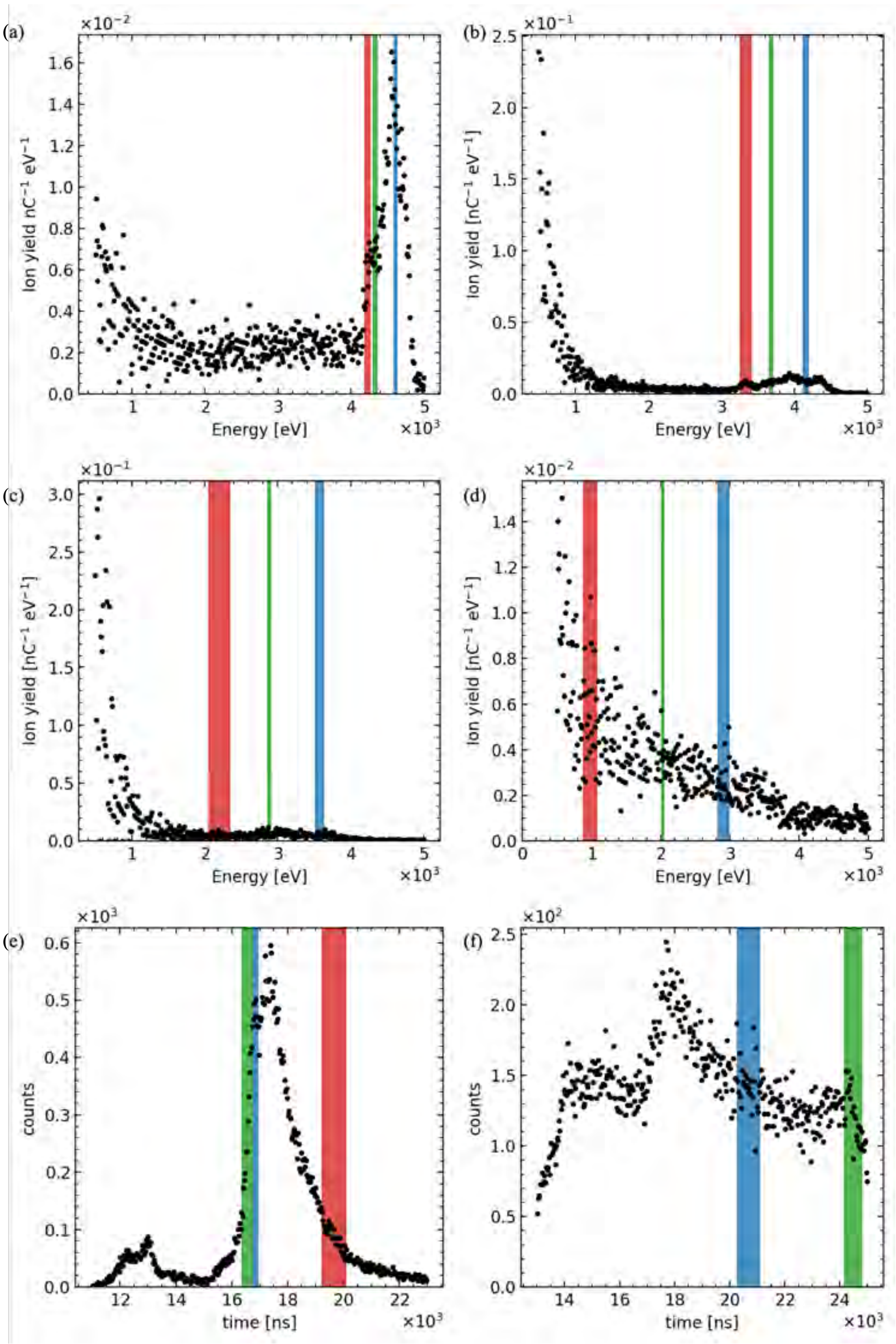

Figure .1: Energy distributions of reflected and recoiled ions and atoms of 5 keV Xe^+ on Ru target taken via ESA over a detection angle of 20° **(a)**, 30° **(b)**, 40° **(c)**, and 50° **(d)**; taken via ToF over a detection angle of 40° **(e)** and 65° **(f)**, and over an incident angle of 15°.

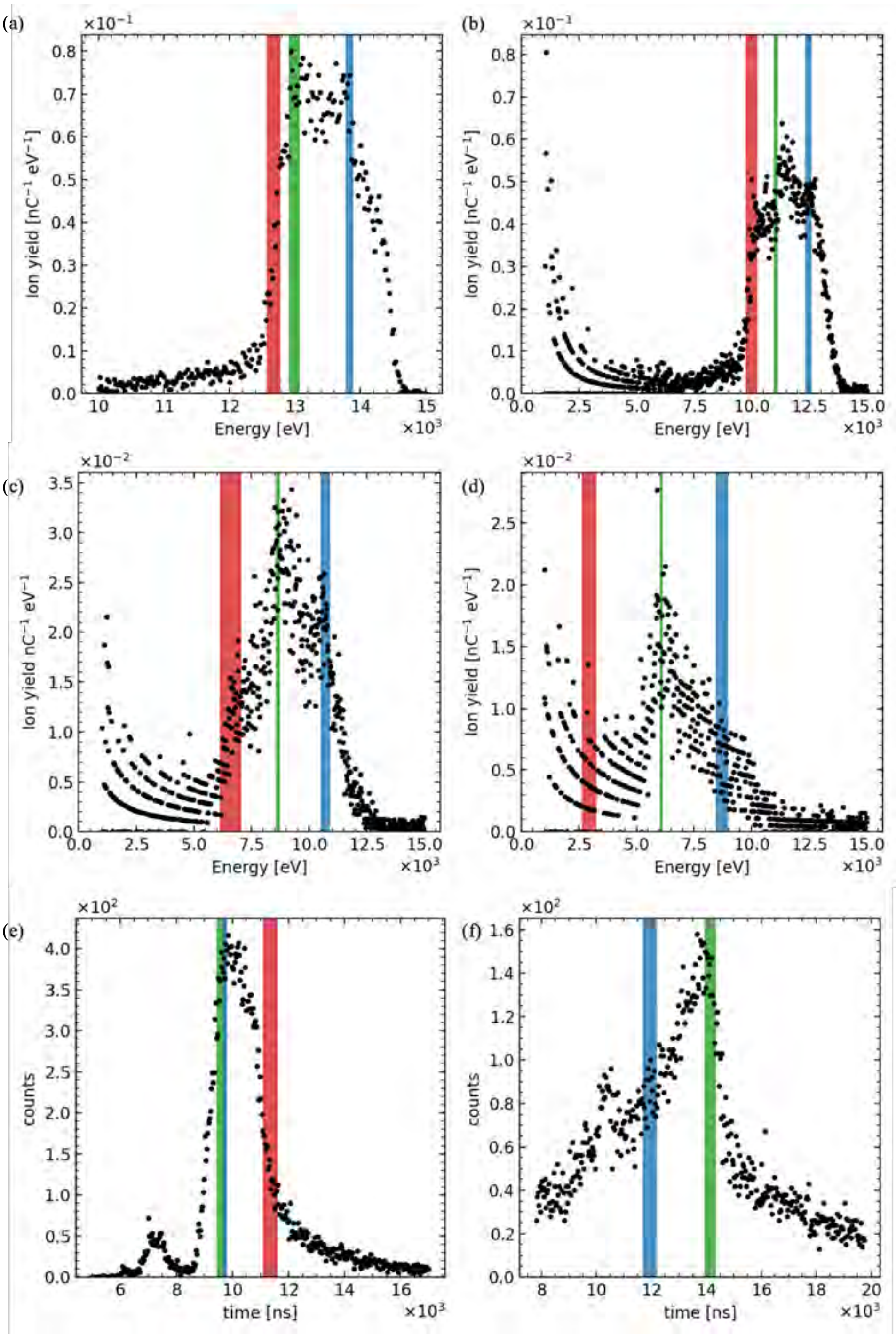

Figure .2: Energy distributions of reflected and recoiled ions and atoms of 15 keV Xe^{3+} on Ru target taken via ESA over a detection angle of 20° **(a)**, 30° **(b)**, 40° **(c)**, and 50° **(d)**; taken via ToF over a detection angle of 40° **(e)** and 65° **(f)**, and over an incident angle of 15°.

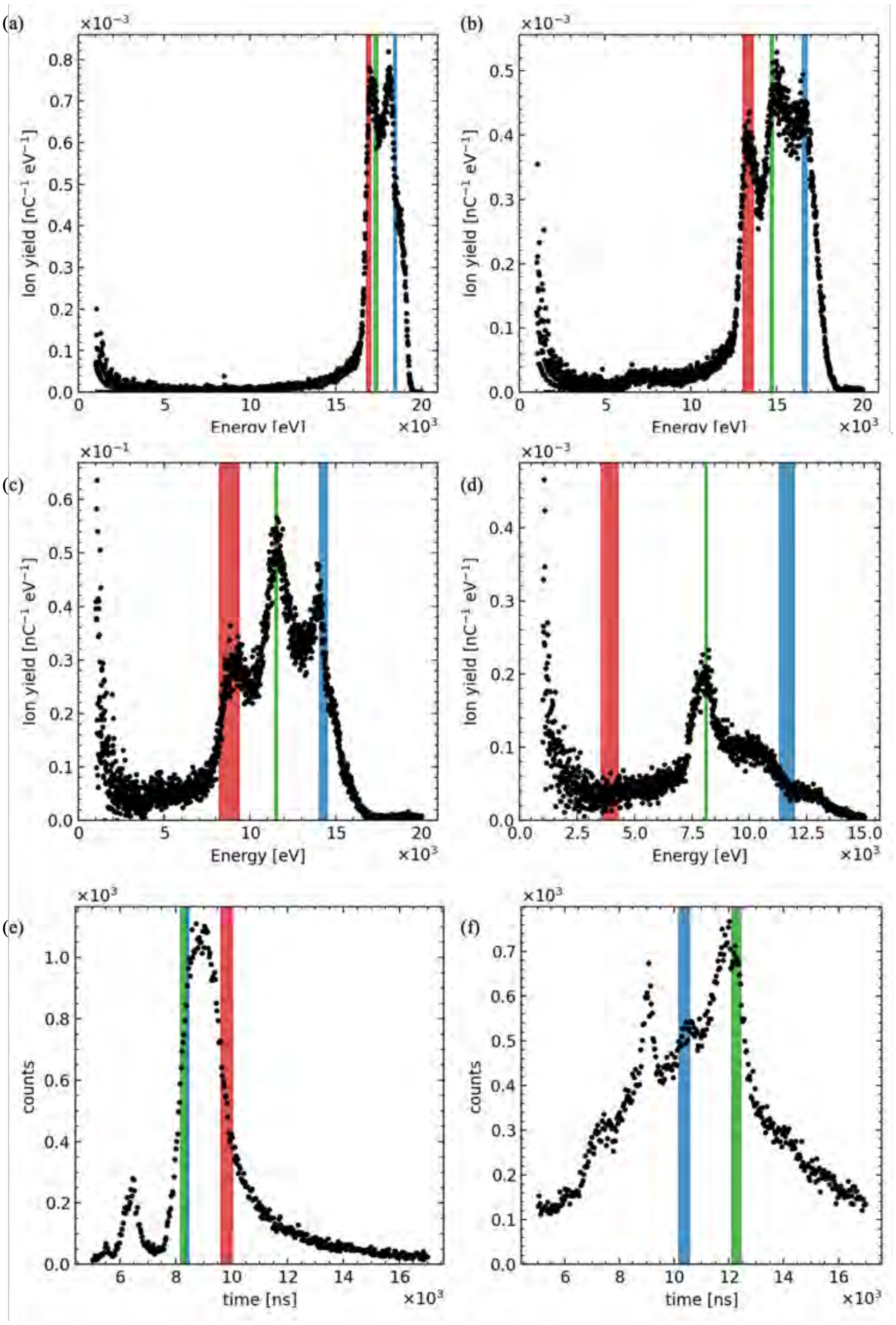

Figure .3: Energy distributions of reflected and recoiled ions and atoms of 20 keV Xe^{2+} on Ru target taken via ESA over a detection angle of 20° **(a)**, 30° **(b)**, 40° **(c)**, and 50° **(d)**; taken via ToF over a detection angle of 40° **(e)** and 65° **(f)**, and over an incident angle of 15°.

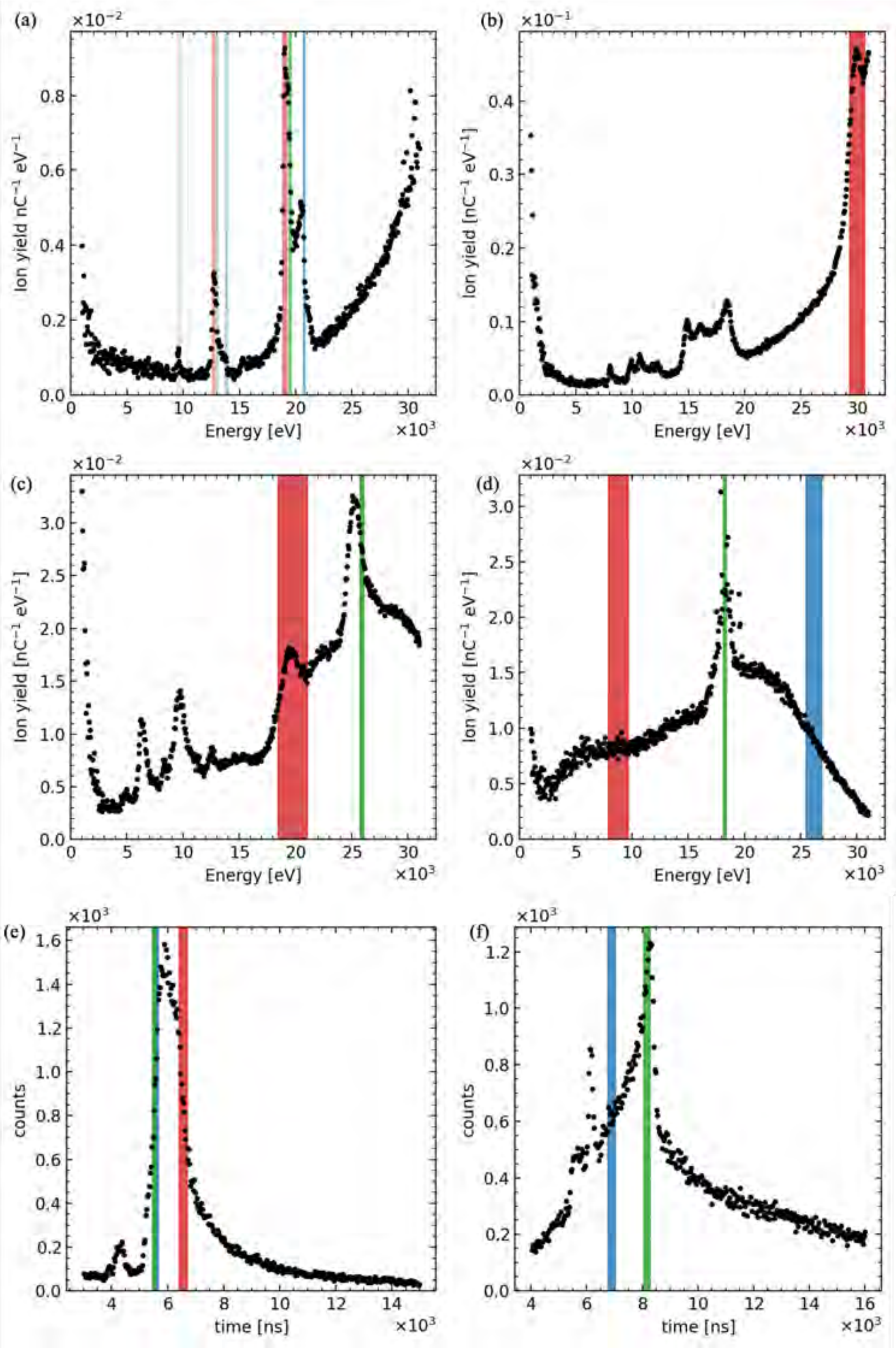

Figure .4: Energy distributions of reflected and recoiled ions and atoms of 45 keV Xe^{3+} on Ru target taken via ESA over a detection angle of 20° **(a)**, 30° **(b)**, 40° **(c)**, and 50° **(d)**; taken via ToF over a detection angle of 40° **(e)** and 65° **(f)**, and over an incident angle of 15°.

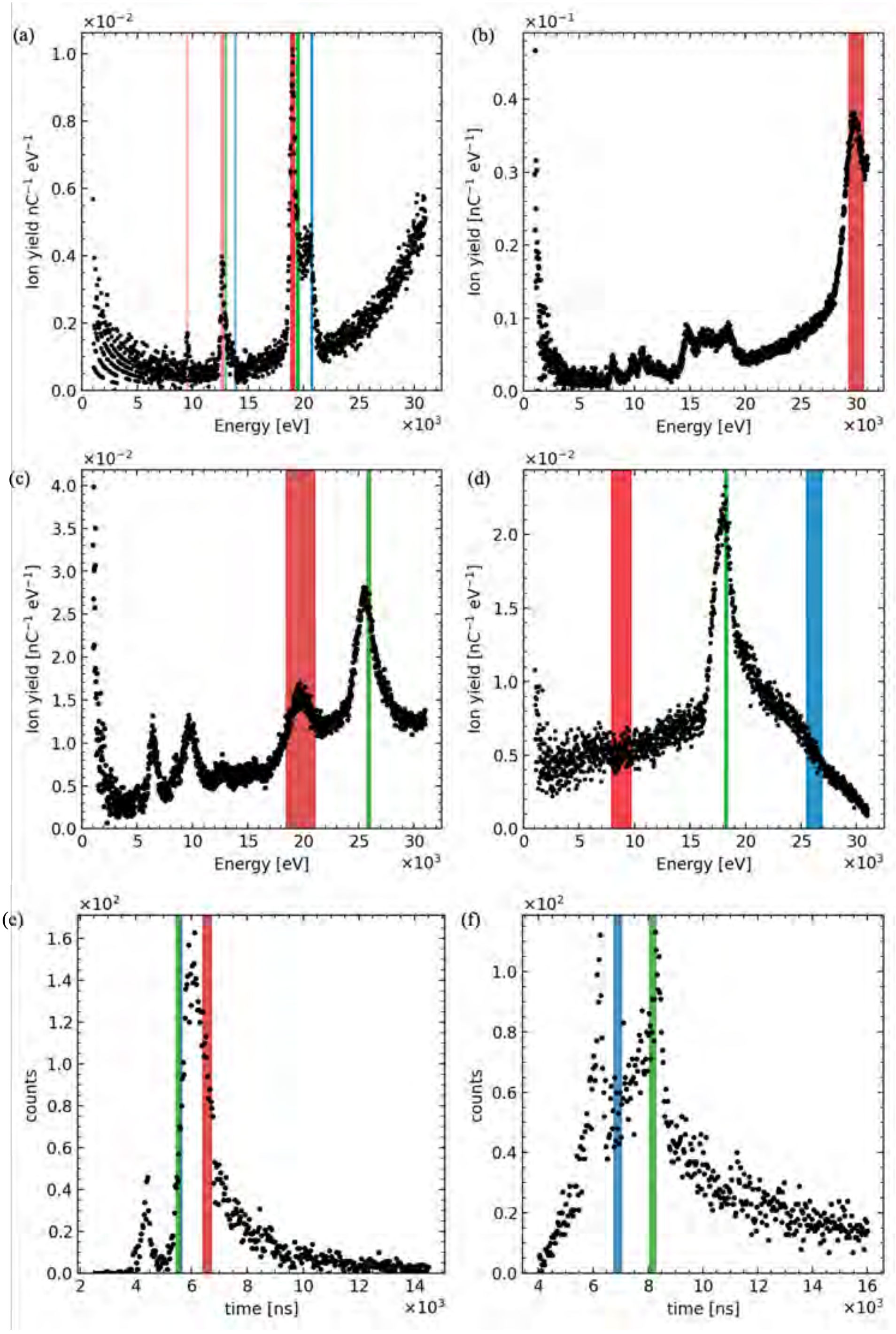

Figure .5: Energy distributions of reflected and recoiled ions and atoms of 45 keV Xe^{4+} on Ru target taken via ESA over a detection angle of 20° **(a)**, 30° **(b)**, 40° **(c)**, and 50° **(d)**; taken via ToF over a detection angle of 40° **(e)** and 65° **(f)**, and over an incident angle of 15°.

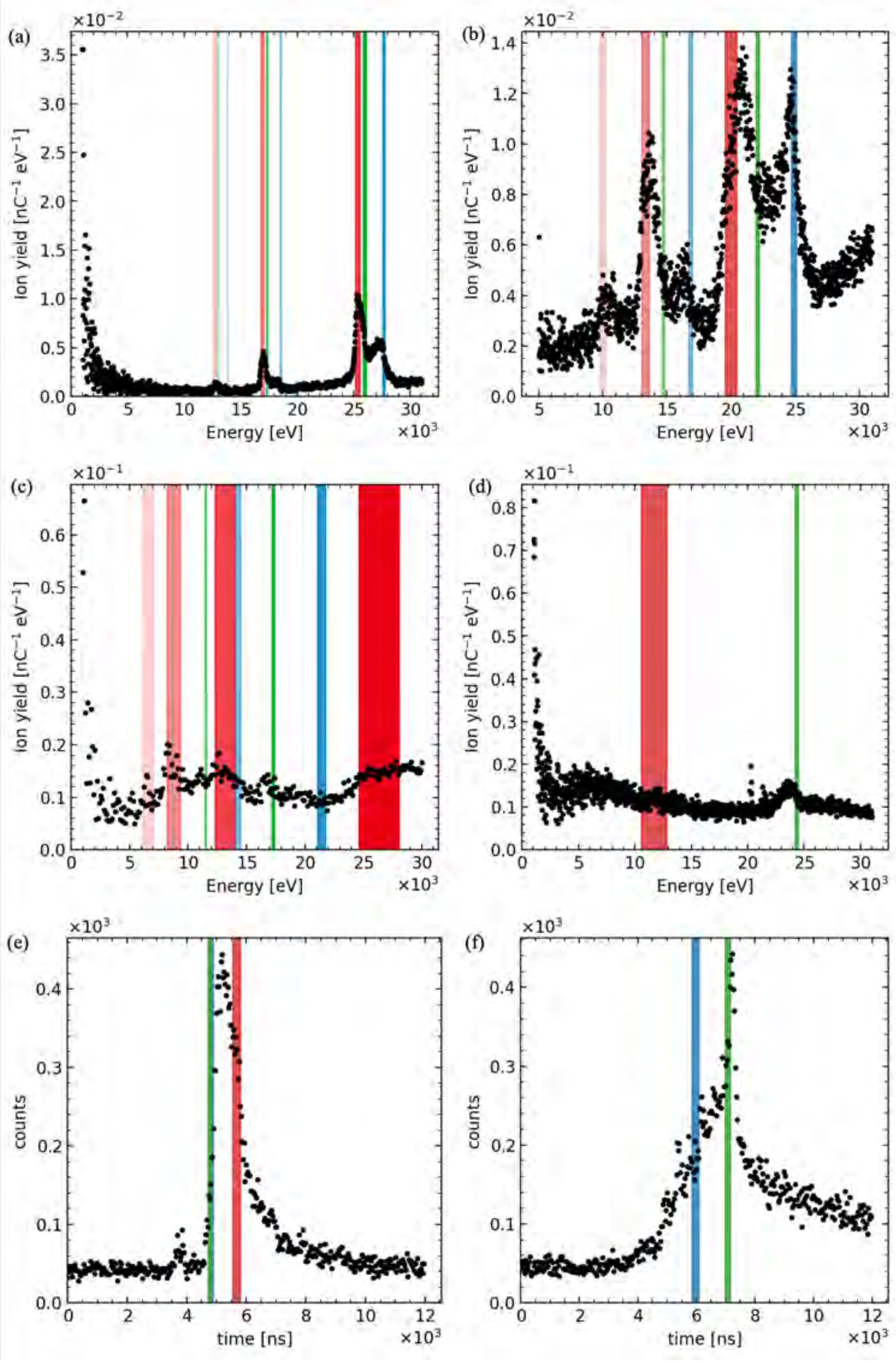

Figure .6: Energy distributions of reflected and recoiled ions and atoms of 60 keV Xe^{4+} on Ru target taken via ESA over a detection angle of 20° **(a)**, 30° **(b)**, 40° **(c)**, and 50° **(d)**; taken via ToF over a detection angle of 40° **(e)** and 65° **(f)**, and over an incident angle of 15°.